This article has been accepted for publication and undergone full peer review but has not been through the copyediting, typesetting, pagination and proofreading process, which may lead to differences between this version and the Version of Record. Please cite this article as **https://doi.org/10.1002/adma.202105007**

Oligoethylene glycol sidechains increase charge generation in organic semiconductor nanoparticles for enhanced photocatalytic hydrogen evolution

Jan Kosco, Soranyel Gonzalez-Carrero, Calvyn T. Howells, Weimin Zhang, Maximilian Moser, Rajendar Sheelamanthula, Lingyun Zhao, Benjamin Willner, Tania C. Hidalgo, Hendrik Faber, Balaji Purushothaman, Michael Sachs, Hyojung Cha, Rachid Sougrat, Thomas D. Anthopoulos, Sahika Inal, James R. Durrant, Iain McCulloch**

Dr. Jan Kosco, Dr. Calvyn T. Howells, Dr. Weimin Zhang, Dr. Rajendar Sheelamanthula, Dr. Hendrik Faber, Dr. Balaji Purushothaman, Prof. Thomas Anthopolous, Prof. Iain McCulloch
King Abdullah University of Science and Technology (KAUST), KAUST Solar Center (KSC), Physical Sciences and Engineering Division (PSE), Thuwal 23955-6900, Kingdom of Saudi Arabia. E-mail: jan.kosco@kaust.edu.sa, iain.mcculloch@chem.ox.ac.uk

Dr. Soranyel Gonzalez-Carrero, Dr. Michael Sachs, Prof. James R. Durrant
Department of Chemistry and Centre for Processable Electronics, Imperial College London, Exhibition Road, London, SW7 2AZ, United Kingdom.

Tania C. Hidalgo, Prof. Sahika Inal
King Abdullah University of Science and Technology (KAUST), Biological and Environmental Science and Engineering Division, Organic Bioelectronics Laboratory, Thuwal, 23955-6900 Saudi Arabia

Dr. Maximilian Moser, Benjamin Willner, Prof. Iain McCulloch
Department of Chemistry, University of Oxford, 12 Mansfield Road, Oxford, OX1 4BH, UK

Dr. Hyojung Cha
Department of Hydrogen & Renewable Energy, Kyungpook National University, Daegu 41566, Republic of Korea

Keywords: photocatalysts, solar fuels, organic semiconductors, nanoparticles, hydrogen

Organic semiconductor nanoparticles (NPs) composed of an electron donor/acceptor (D/A) semiconductor blend have recently emerged as an efficient class of hydrogen evolution photocatalysts. We demonstrate that employing conjugated polymers functionalized with (oligo)ethylene glycol sidechains in NP photocatalysts can greatly enhance their H_2 evolution efficiency compared to their non-glycolated analogues. The strategy is broadly applicable to a range of structurally diverse conjugated polymers. Transient spectroscopic studies show that glycolation facilitates charge generation even in the absence of a D/A heterojunction, and further suppresses both geminate and non-geminate charge recombination in D/A NPs. This results in a high yield of photogenerated charges with lifetimes long enough to efficiently

drive ascorbic acid oxidation, which is correlated with greatly enhanced H_2 evolution rates in the glycolated NPs. Glycolation increases the relative permittivity of the semiconductors and facilitates water uptake. Together, these effects may increase the high frequency relative permittivity inside the NPs sufficiently to cause the observed suppression of exciton and charge recombination responsible for the high photocatalytic activities of the glycolated NPs.

1. Introduction

Solar irradiation is an abundant source of renewable energy. However, the conversion of solar energy into a form that can be stored and used on demand remains a major challenge. Photocatalytic water splitting to generate hydrogen; a versatile, clean burning fuel, is a potential solution to this problem.[1] A photocatalyst absorbs light and converts it to photogenerated charges that can be used to drive redox reactions on its surface. Most research has so far focused on photocatalysts fabricated from wide bandgap semiconductors such as TiO_2,[2,3] $SrTiO_3$, [4,5] and carbon nitride (CN). [6–8] However, photocatalysts fabricated from these semiconductors are primarily active under ultraviolet wavelengths, which contain <5% of solar energy.[1] This limits their maximum solar to hydrogen efficiency (η_{STH}) to below the 5-10% threshold deemed necessary for commercial viability.[9] More recently, photocatalysts fabricated from a diverse range of organic semiconductors such as linear conjugated polymers, [10,11] crosslinked microporous polymers, [12–14] and covalent organic frameworks[14–17] have been developed.[18] The frontier molecular orbital energy levels of these semiconductors can be synthetically tuned to absorb a broader spectrum of solar irradiation while retaining suitable energy level alignments to drive the H_2 evolution reaction (HER) and/or the O_2 evolution reaction (OER). This enables them to achieve a maximum theoretical η_{STH} >10%.[1,18] Promising efficiencies have been achieved, however further work is required to raise efficiencies towards this theoretical limit. Most studies that have focused on enhancing the photocatalytic H_2 evolution efficiency of organic semiconductor photocatalysts require the presence of sacrificial hole scavengers such as triethylamine (TEA) or ascorbic acid (AA). [11,19–21] These hole scavengers extract photogenerated holes from the semiconductor, which enables the photogenerated electrons to drive the HER. Some hole scavengers, such as high concentrations of TEA, can also facilitate charge separation at the semiconductor/electrolyte interface by extracting photogenerated holes directly from polymer excitons on the ps timescale.[11,20] This process is known as “reductive quenching” and is often the dominant mechanism of charge separation in photocatalysts composed of a single semiconductor.[22] Increasing the hydrophilicity of conjugated polymer photocatalysts through the incorporation of polar backbone units containing sulfone groups and/or hydrophilic glycol sidechains has recently emerged as an effective strategy for improving photocatalytic efficiency.[20,23] Increased hydrophilicity makes the semiconductor more accessible to

sacrificial hole scavengers which enhances charge separation via reductive quenching and can produce a concomitant increase in the photocatalyst's HER rate.[20,24]

Charge separation within an organic photocatalyst can also be induced by fabricating NP photocatalysts composed of a blend of two semiconductors with a type II energy level offset. Exciton dissociation can occur at the electron donor/acceptor (D/A) heterojunction within the NPs which can enable D/A NPs to achieve greatly enhanced HER rates compared to NPs composed of the individual semiconductors.[18,21,25] Because exciton dissociation can take place inside the D/A NPs, these photocatalysts do not rely on reductive quenching by a hole scavenger to generate catalytically active charges. This enables them to operate efficiently even in the presence of lower concentration hole scavengers which extract holes from the semiconductor on the µs timescale, such as AA .[21] Furthermore, by using organic semiconductors with complementary absorptions, D/A NPs can be designed to absorb throughout the UV-Visible spectrum.[26]

As well as enhancing hydrophilicity, the introduction of polar glycol side-chains in conjugated polymers and fullerene derivatives has been shown to increase their relative permittivity (dielectric constant, ε_r).[27–29] This has been proposed to be responsible for reduced non-geminate recombination and increased charge carrier lifetimes in bulk heterojunction solar cells, due to a reduced coulombic attraction between photogenerated polarons.[30] However, glycolation has not been shown to enhance charge generation or exciton dissociation in conjugated polymers. This is possibly because glycol sidechains cannot reorient fast enough to reduce the coulombic attraction between photogenerated electrons and holes in excitons (the exciton binding energy) before the excitons recombine.[31–33]

In this work, we explored the use of a range of conjugated polymers with glycol sidechains in NP H_2 evolution photocatalysts. We demonstrate that glycolation greatly enhances the H_2 evolution rate of NP photocatalysts composed of the individual conjugated polymers and their blends with the electron acceptors $PC_{71}BM$ or oIDTBR. NP photocatalysts composed of a single glycolated semiconductor achieved greatly enhanced HER rates compared to their non-glycolated analogues. This HER rate enhancement occured even when the glycolated and non-glycolated NPs had similar size distributions and when the relatively slow hole scavenger AA was used. Photophysical characterization revealed that glycolation can promote ultrafast charge separation and suppress both geminate and nongeminate recombination, leading to a higher yield of long-lived photogenerated charges within the glycolated NPs even in the absence of a D/A heterojunction, or the addition of Pt or a sacrificial hole scavenger. This was

attributed to a higher ε_r of the environment within the glycolated NPs, endowed by the high polarity of the glycol sidechains and possibly also their hydrophilicity that enables the uptake of high permittivity water molecules from the surrounding aqueous phase. NPs composed of a blend of an electron donor polymer and a small molecule electron acceptor introduced a D/A heterojunction within the NPs that further promoted exciton dissociation at the D/A interface. Glycolation of the donor polymer in these D/A NPs further reduced rates of geminate and non-geminate charge recombination. This increased the yield of long-lived polarons that remained within the NPs on timescales that enable H_2 evolution and hole scavenging by AA and led to a further dramatic enhancement of the HER rate.

2. Results

Analogues of the conjugated polymers indacenodithiophene–benzothiadiazole (IDTBT), poly(9,9-dioctylfluorene-alt-benzothiadiazole) (F8BT) and poly[4,8-bis(5-(2-ethylhexyl)thiophen-2-yl)benzo[1,2-b;4,5-b']dithiophene-2,6-diyl-alt-(4-(2-ethylhexyl)-3-fluorothieno[3,4-b]thiophene-)-2-carboxylate-2-6-diyl)] (PTB7-Th) bearing either alkyl sidechains (IDTBT, F8BT, PTB7-Th) or oligoethylene glycol sidechains (gIDTBT, FgBT, gPTB7-Th) were synthesized (Synthetic procedures can be found in the supporting information). These polymers were chosen because of their strong visible light absorption, solubility, and suitable highest occupied molecular orbital (HOMO) and lowest unoccupied molecular orbital (LUMO) energy levels (**Figure 1**). All the polymers had HOMO energy levels deep enough to drive ascorbic acid (AA) oxidation and LUMO levels shallow enough to drive proton reduction. Furthermore, they could also form a type II electron donor/acceptor (D/A) heterojunction with at least one of the electron acceptors (oIDTBR or $PC_{71}BM$) used in this study.

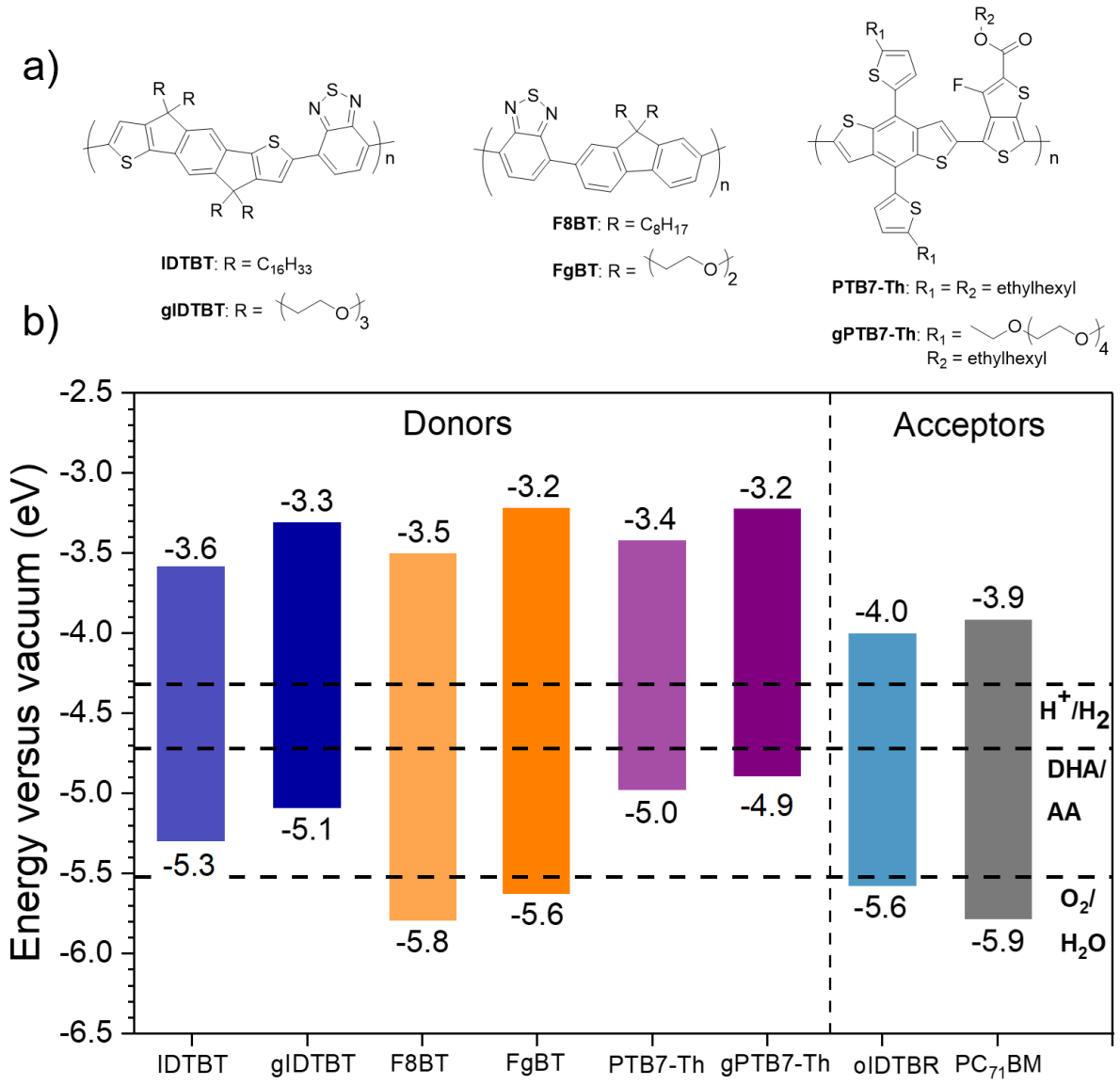

Figure 1: Chemical structures, energy levels, and absorption spectra. **a)** chemical structures of IDTBT, gIDTBT, F8BT, FgBT, PTB7-Th and gPTB7-Th. **b)** Frontier molecular orbital energy levels measured using a combination of photoelectron emission spectroscopy in air (PESA) and UV-visible absorption spectroscopy of dry films of IDTBT, gIDTBT, F8BT, FgBT, PTB7-Th, gPTB7-Th, oIDTBR PC_7BM. The exciton binding energy is assumed to be negligible. The dashed lines correspond to the proton reduction potential (H^+/H_2), water oxidation potential (O_2/H_2O) and the calculated potential of the two-hole oxidation of ascorbic acid to dehydroascorbic acid in solution (DHA/AA) at pH 2 (the experimentally

measured pH of 0.2 mol l^{-1} ascorbic acid).[23] All energy levels and electrochemical potentials are expressed relative to vacuum (using -4.44 V versus vacuum = 0 V versus SHE).[34]

Nanoparticles (NPs) composed of the individual semiconductors and their blends with either oIDTBR or $PC_{71}BM$ were prepared using the miniemulsion method, and the NP size distributions were measured by dynamic light scattering (**Figure S1, Tables S1-S3**).[35] The H_2 evolution rate of each NP batch was measured in the presence of photodeposited Pt, which served as a H_2 evolution co-catalyst, and the sacrificial hole scavenger AA (**Figure 2**).

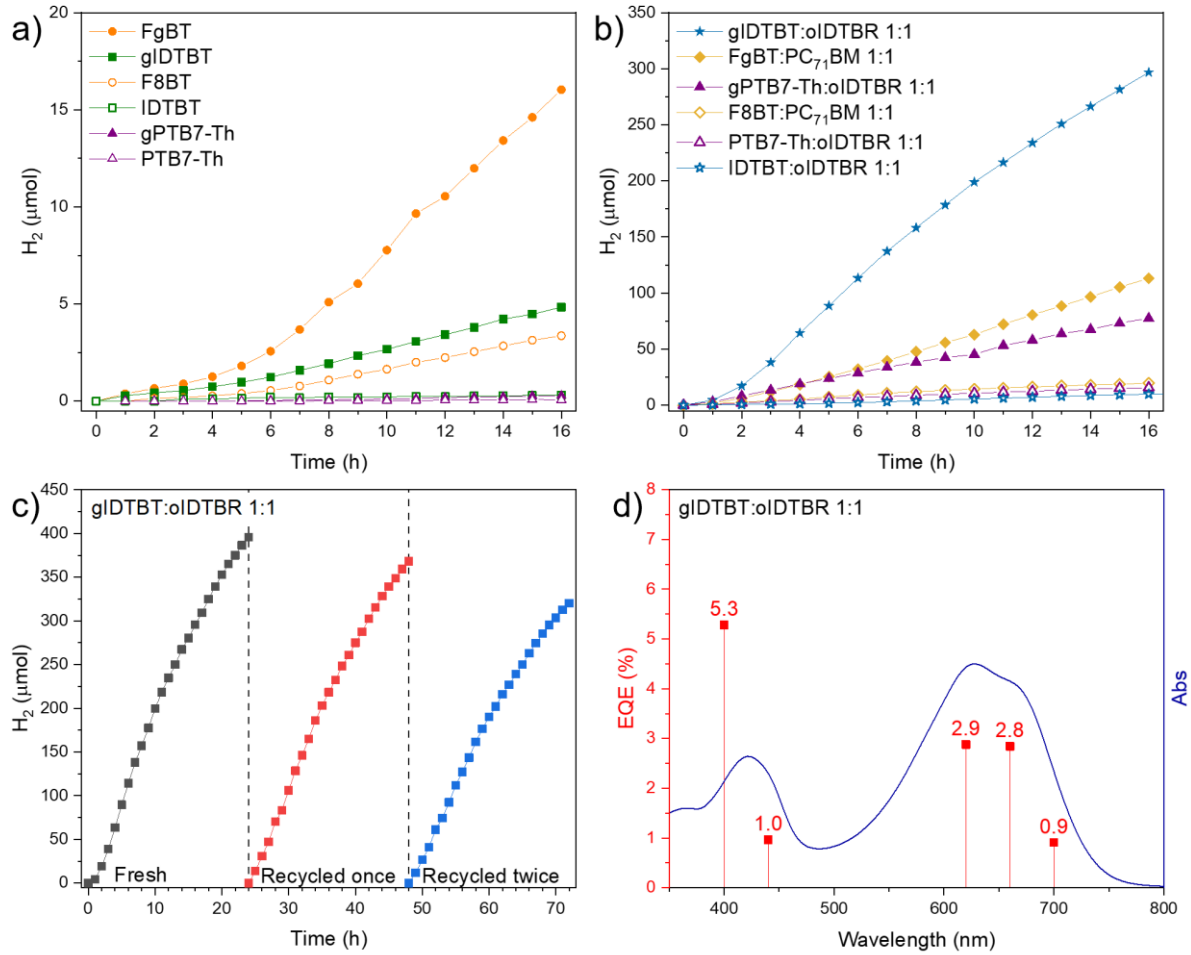

Figure 2: H_2 evolution and external quantum efficiencies (EQEs). H_2 evolution vs. time of **a)** NPs composed of the individual donor polymers **b)** NPs containing a D/A heterojunction formed of a 1:1 blend by mass of a donor polymer matched with either oIDTBR or $PC_{71}BM$

electron acceptors. Data presented are the average of 3 repeat runs. **c)** Stability and recyclability test of gIDTBT:oIDTBR NPs. Dashed lines indicate the times at which the reactor was evacuated to remove H_2 and the NPs were recycled. **d)** Absorption spectrum and EQEs of gIDTBT:oIDTBR NPs at 400, 440, 620, 660, 700 nm. H_2 evolution conditions: 1 mg nanoparticles, 0.2 mol l^{-1} ascorbic acid (12 ml), pH 2, 10 µg (10 wt.%) Pt, AM1.5g solar simulator at 100 $mWcm^{-2}$ (1 sun), 4.41 cm^2 illumination area.

Replacing alkyl sidechains with glycol sidechains increased the H_2 evolution reaction (HER) rate of NPs formed from gIDTBT by a factor of 16, of FgBT by a factor of 5, and of gPTB7-Th by a factor of 4 compared to their non-glycolated analogues (Figure 2a). These HER rate increases are comparable to those observed upon the replacement of alkyl sidechains with glycol sidechains in other conjugated polymers,[20,29] and can be attributed to enhanced charge generation and increased polaron lifetimes in the glycolated semiconductors due the increased ε_r afforded by the glycol sidechains, based on the analysis below. However, the HER rates of NPs composed of the individual semiconductors remained low. NPs composed of D/A blends (Figure 2b) achieved HER rates an order of magnitude higher than those composed of the individual donor polymers, and all D/A NPs that contained a glycolated semiconductor achieved a higher HER rate than those containing their non-glycolated analogues. The highest HER rate of 4.21 $\mu molh^{-1}cm^{-2}$ (18.5 $mmolh^{-1}g^{-1}$) over 16 h was achieved by the gIDTBT:oIDTBR NPs, which is a 30-fold increase compared to the non-glycolated IDTBT:oIDTBR NPs. An extended stability test (Figure 2c) revealed that the gIDTBT:oIDTBR NPs loaded with 10 wt.% Pt could generate H_2 for $\geq$ 72 h, producing 1.1 mmol of H_2 in 72 h. They retained 93% of their original 24 h performance during the second 24 h cycle and 81% during the third 24 h cycle. Between cycles the reactor was evacuated, the NPs were removed from the reaction medium with the aid of a centrifugal filter and fresh AA was added (see supplementary information for details). The gIDTBT:oIDTBR NPs loaded

with 10 wt.% Pt were active throughout the visible spectrum and achieved photon-to-hydrogen conversion EQEs of approximately 3% at 620-660 nm (Figure 2d). The greatest HER rate increase in NPs composed of the individual semiconductors and their blends was achieved upon the replacement of IDTBT with gIDTBT. Detailed functional characterization hereafter therefore focused primarily on the effect of replacing the alkyl sidechains on IDTBT with glycol sidechains in NPs composed of the individual IDTBT and gIDTBT polymers and their blends with oIDTBR. As can be seen from Figures 2b-c, at longer times the HER rates become nonlinear. We have evaluated possible causes of this nonlinearity in detail, as shown in figures S28-30 and were able to rule out NP degradation, aggregation, or co-catalyst degradation. The primary cause of the nonlinearity appears to be AA depletion during the course of each run.

The NP morphology was characterized by cryogenic Transmission Electron Microscopy (cryo-TEM, **Figure 3**). NPs formed of pure gIDTBT displayed an amorphous internal morphology, while oIDTBR NPs were highly crystalline with a periodic lattice spacing of approximately 1.7 nm clearly visible as alternating lines of high and low electron density. This spacing corresponds to a diffraction peak at approximately q = 0.41 $Å^{-1}$ (d = 15.3 Å) observed by grazing incidence x-ray diffraction in an annealed oIDTBR thin film.[36] The gIDTBT:oIDTBR NPs (Figure 3 c) and the IDTBT:oIDTBR NPs (Figure 3 e) both displayed a core-shell morphology with a crystalline oIDTBR core domain encapsulated by an amorphous IDTBT or gIDTBT shell. The oIDTBR domains retained their characteristic 1.7 nm lattice spacings, and the constant lattice orientation throughout the NP cores suggest that they are composed of a single oIDTBR crystal. The NP morphology was unchanged after 20 h H_2 evolution, and Pt was photodeposited in the form of NPs with a 2-5 nm diameter on both the gIDTBT:oIDTBR NPs (Figure 3 d) and the IDTBT:oIDTBR NPs (Figure 3 e). The IDTBT:oIDTBR and the gIDTBT:oIDTBR NPs also had similar size distributions and the same 70 nm Z-average hydrodynamic diameter (Figure S1 Table S1). From this it can be

concluded that the enhanced HER rate of the gIDTBT:oIDTBR NPs did not originate from an improved NP morphology or a smaller particle size as has been reported previously for photocatalysts formed from a single glycolated semiconductor.[20,29]

Figure 3: Bright field cryo-TEM images of nanoparticles. **a)** gIDTBT **b)** oIDTBR **c)** gIDTBT:oIDTBR 1:1 before, and **d)** after photodeposition of 10 wt.% Pt and 20h H_2 evolution. **d)** IDTBT:oIDTBR 1:1 before, and **f)** after photodeposition of 10 wt.% Pt and 20h H_2 evolution. Profiles of the periodic spacings in the rectangles in images b-f are available in Figures S4-S6. Note: The dark areas at the top of images c and d originate from the TEM grid.

To probe the photophysical origin of the increased HER rates in the NPs with glycol side chains, photoluminescence (PL) and transient absorption spectroscopy (TAS) were employed, focusing on the effect of glycolating IDTBT. We first considered the effect of glycolation on neat polymer NPs. The PL spectrum of IDTBT NPs showed a broad emission with maximum at 725 nm; for gIDTBT NPs this emission is red shifted and six times lower in amplitude, indicating that glycolation strongly suppressed radiative exciton recombination (**Figure 4a**). Ultrafast transient absorption spectra for both IDTBT and gIDTBT NPs are shown in Figure 4b, c and S7. For both NPs, the initial (1 ps) spectrum exhibits a ground state bleach at 670 nm (Figure S7) and broad photoinduced absorption at 1300 nm, assigned to IDTBT singlet excitons, in agreement with previous studies of IDTBT films.[37] Interestingly, the NIR transient spectra of gIDTBT evolve into a band with a maximum at 1050 nm over the first 100 ps; this band is much less pronounced for non-glycolated IDTBT NPs. This 1050 nm absorption feature was also observed in transient spectra of gIDTBT NPs at longer time scales (μs-ms), exhibiting power law decay kinetics and slow quenching by molecular oxygen,

indicative of its assignment to long lived gIDTBT polarons. (Figures S8 and S9). In contrast, for non-glycolated IDTBT NPs, only a low amplitude, shorter lived (µs) and strongly oxygen quenched absorption signal was observed, indicative of IDTBT triplet excitons (Figure S9).[38] Deconvolution of the exciton and polaron signals observed for gIDTBT NPs on ultrafast timescales indicates the formation of this polaron signal with a 8 ps halftime, concomitant with the decay of gIDTBT singlet excitons (Figure 4d), indicative of rapid charge generation, and consistent with the strongly suppressed PL of gIDTBT NPs. This polaron signal was observed to exhibit a fluence-independent decay with a half time of ~ 1 ns (Figure S10), indicative of a significant proportion of geminate recombination of bound charge pairs (i.e. intermolecular charge transfer states). These results indicate that the modification of IDTBT with glycol side chains results in surprisingly efficient exciton separation even in the absence of a D/A heterojunction, or the addition of Pt or a sacrificial hole scavenger. The enhanced charge generation in the gIDTBT NPs results in a higher yield of catalytically active charges and is responsible for their enhanced HER rate compared to their non-glycolated analogues.

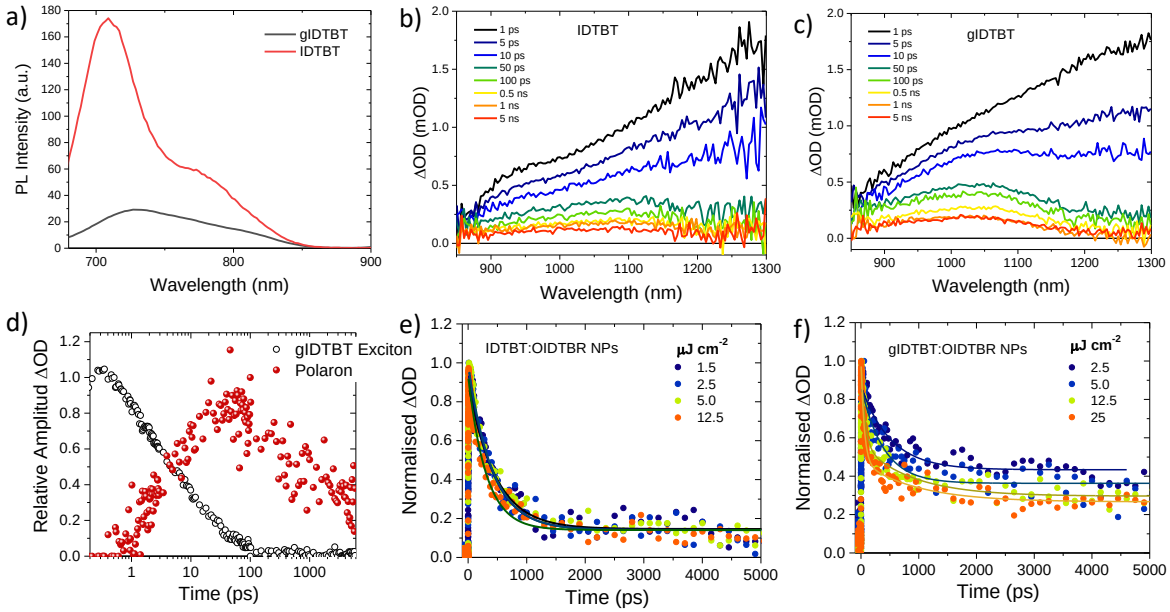

Figure 4. Photophysics of NPs in aqueous suspension. a) Steady state photoluminescence spectra of gIDTBT and IDTBT NP suspensions, excited at 650 nm. b,c) Ultrafast transient absorption spectra of IDTBT (b) and gIDTBT NP suspensions (c) at different delay times. d)

Deconvoluted transient absorption kinetics of gIDTBT excitons and polarons obtained via global analysis (see SI for details) of the data shown in (c). e,f) Transient absorption kinetics representing polaron decay kinetics at different fluences in IDTBT:oIDTBR (e) and gIDTBT:oIDTBR (f) NP suspensions, probed at 750 nm. Full lines are monoexponential fits to the data with an offset. All transient absorption data were recorded following 650 nm excitation using a fluence of 5 μJ cm^{-2} unless indicated otherwise.

We now focus on transient absorption studies of the exciton and polaron kinetics in D/A NPs with oIDTBR (Figures 4 e, f, S11-S15). For both IDTBT:oIDTBR and gIDTBT:oIDTBR NPs, singlet exciton signals were strongly quenched within 1 ps, with polaron absorption at 1050 nm dominating the NIR transient spectra, indicative of efficient, sub-picosecond exciton separation to form charges in both NPs. However, the two NPs differ significantly in the decay dynamics of these charges. IDTBT:oIDTBR NPs showed a rapid (~500 ps) and fluence-independent decay kinetics, indicative of the geminate (monomolecular) recombination of photogenerated charge transfer (CT) states, with only a low yield (~10%) of long lived, separated charges. Analogous, field dependent geminate recombination losses have been observed in organic photovoltaic devices employing oIDTBR, and were attributed to a small energy offset and morphological effects.[39,40] In contrast, gIDTBT:oIDTBR NPs exhibited slower, fluence dependent decay kinetics, indicative of the bimolecular recombination of spatially separated polarons, and indicating that glycolation results in the strong suppression of CT state geminate recombination. μs-ms transient absorption data indicate a higher yield of longer lived charges in gIDTBT:oIDTBR NPs compared to IDTBT:oIDTBR NPs (Figure S15), further confirming that glycolation results in a retardation of charge recombination losses. It can be concluded that glycolation substantially enhances the efficiency of charge separation in these D/A NPs, wich is consistent with the observed higher rates of H_2 evolution.

The data shown in Figure 4 indicate that glycolation results in a substantive suppression of exciton and polaron recombination in these NPs. This effect is observed even in neat gIDTBT NPs, which exhibit remarkably efficient charge generation. However, in the absence of a D/A heterojunction, the charges generated primarily undergo geminate recombination on the nanosecond timescale. This is too fast for efficient hole scavenging by AA, which is consistent with the low H_2 yield from NPs composed of pure gIDTBT. In the gIDTBT:oIDTBR and the IDTBT:oIDTBR NPs, exciton separation is efficient both with and without glycolation due to the presence of a D/A heterojunction within the NPs. The effect of glycolation in the gIDTBT:oIDTBR NPs is primarily to suppress both geminate and non-geminate recombination. The resultant generation of long lived charges enables efficient hole scavenging by AA on the μs timescale (Figure S15), and the remarkably efficient photocatalytic H_2 evolution of the gIDTBT:oIDTBR NPs compared to their non-glycolated analogues. These data also confirm that the enhanced HER rates of the glycolated NPs did not originate simply from an increased availability of their hydrophilic surface to AA, because AA does not extract holes from the NPs on a timescale fast enough to efficiently dissociate polymer excitons. Hole extraction by AA takes place on the μs timescale (Figure S15), which is several orders of magnitude slower than the typical timescale of singlet exciton recombination in organic semiconductors (ps-ns).[11,20,22] Rather, glycolation results in a higher yield of long lived photogenerated charges capable of driving AA oxidation and H_2 evolution.

Glycolation has also been reported to enhance the performance of dibenzo[b,d]thiophene sulfone polymer photocatalyst dispersions, attributed to a higher wettability and an increased local dielectric aiding charge stabilization, consistent with the results herein. However with this sulphone polymer, long lived charge generation was only observed in the presence of 30% TEA, with glycolation increasing the efficiency hole scavenging,[20] as well as increasing the lifetime of the resultant electron polarons. The results herein indicate that glycolation can enhance the charge separation and retard charge recombination of the polymer NPs even in the

absence of a sacrificial electron donor, by impacting on the intrinsic, ultrafast photophysics of these NPs. This impact of glycolation on the ultrafast exciton and charge dynamics is particularly striking, and contrasts with studies of the impact of glycolation on spin coated, dry polymer films and BHJs, where extensive studies have reported impact only on slower (typically ns-ms) charge carrier dynamics,[27,31,32,41,42] as discussed further below.

Suppressed charge recombination has been reported when glycolated semiconductors were employed in organic solar cells, as a result of their enhanced relative permittivities compared to their non-glycolated analogues.[43–45] An increased ε_r reduces the coulombic attraction between photogenerated electrons and holes, and can result in reduced recombination and longer charge carrier lifetimes in organic semiconductor films.[30,45] Measuring the ε_r of the polymers used in this study **(Figure 5a)** in dry films revealed that glycolation increased the ε_r of gIDTBT by a factor of 2.7, of FgBT by a factor of 1.6, and of gPTB7-Th by a negligible amount compared to their non-glycolated analogues. These increases in relative permittivity can be attributed to the presence of C-O dipoles on the glycol sidechains which can readily reorient in response to an electric field and thus better shield coulombic fields between photogenerated charges.[27] Only three out of the four alkyl sidechains on the PTB7-Th repeat unit were replaced with glycol sidechains in gPTB7-Th, which may be why glycolation only resulted in a negligible increase of the ε_r of gPTB7-Th compared to PTB7-Th.

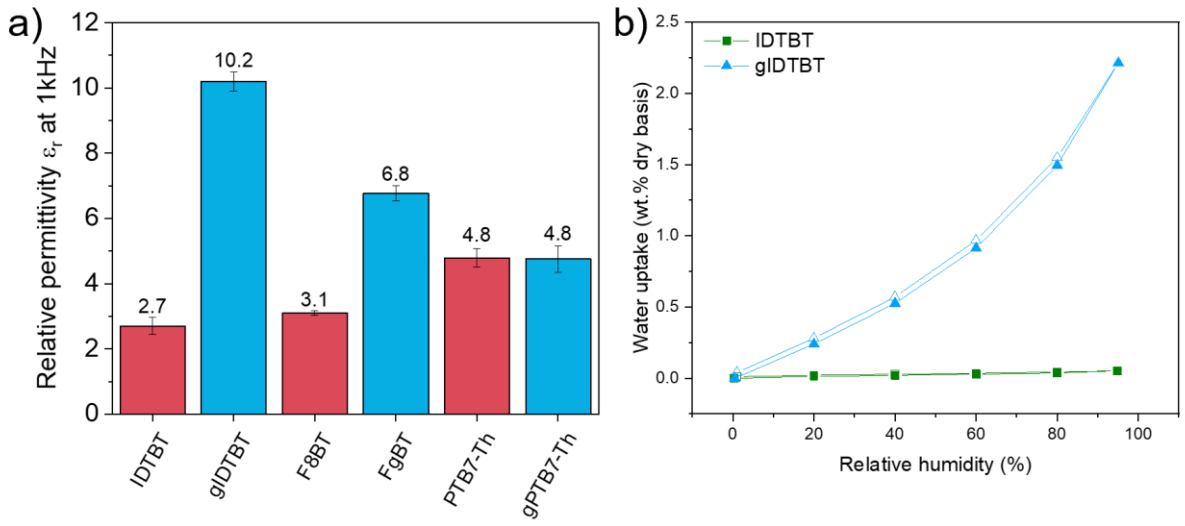

Figure 5: Relative permittivities and water uptake. **a)** Relative permittivity at 1kHz of dry films of the donor polymers used in this study. **b)** water vapour adsorption isotherms of IDTBT and gIDTBT. Full symbols represent adsorption and empty symbols represent desorption.

Glycolation of single conjugated polymers has been shown to increase the polymers' affinity to water, with lower water contact angles and higher water adsorption compared to their alkyl side chain analogues.[20] Here glycolation was also found to enhance the hydrophilicity of all three conjugated polymers, as evidenced by the lower water contact angles of gIDTBT, FgBT, and gPTB7-Th (67°, 86°, 79° respectively) compared to IDTBT, F8BT, and PTB7-Th (105°, 99°, 108° respectively) (Figure S16, Table S4). Furthermore, dynamic water vapour sorption measurements (Figure 5b) revealed that glycolation greatly increased the ability of gIDTBT to adsorb water. At 95% relative humidity, the hydrophilic gIDTBT polymer achieved a water vapour uptake of 2.2% compared to just 0.05% for IDTBT, a more than 40-fold enhancement. The type III gIDTBT water adsorption isotherm displays an exponential increase in water uptake with increasing relative humidity that is characteristic of multi-layer adsorption.[46,47] Quartz crystal microbalance measurements on thin films of IDTBT and gIDTBT (Figure S19) revealed that upon immersion in water (or 0.2 M AA), the mass of gIDTBT increased by

120%. This suggests that the ingress of liquid water into the hydrophilic gIDTBT film caused the polymer to swell.[20,48] The mass of the IDTBT film also increased upon water immersion although, with a mass increase of only 20%, by substantially less than the gIDTBT film. Nevertheless, this is surprisingly high considering the hydrophobicity and low water vapour uptake of IDTBT. It is therefore likely that this relatively small mass increase originated from voids in the IDTBT film being filled by water, as has been previously reported,[49] rather than by water swelling the film. This is supported by atomic force microscopy measurements (Figure S20) which show a negligible increase in the thickness of an IDTBT film upon water immersion, compared to an 11% increase for a gIDTBT film.

Glycolation of dry organic semiconductor films typically only affects their low frequency (up to 1MHz) dielectric response.[32] Therefore, in dry organic semiconductor films, glycolation can retard charge recombination mechanisms that take place on the μs timescale, such as non-geminate recombination, but typically has little impact on exciton and charge-transfer state separation, which take place on the ps-ns timescale.[32,45] However, the observation that glycolation of our NP photocatalysts in water enhances exciton / charge transfer state separation, both in the presence and absence of a D/A heterojunction, suggests that glycolation of these NPs also enhances their high frequency (GHz) relative permittivity. This can most likely be related to the enhanced water uptake of these NPs.[20] Water retains a relative permittivity of >50 at frequencies up to 10 GHz, and 7-8 at frequencies up to 1 THz.[50] The presence of water molecules in the polymer matrix could therefore yield an enhanced high frequency dielectric response, capable of reducing the coulomb attraction of both excitons and charge transfer states on the ps-ns timescale.[50,51] Whilst further work is necessary to confirm this, it is apparent that the enhanced generation of long-lived charges observed with glycolation correlates with the enhanced H_2 evolution rates of glycolated NP photocatalysts.

3. Conclusion

We have demonstrated that glycolation is an effective strategy to enhance the photocatalytic efficiency of NP H_2 evolution photocatalysts. The strategy is broadly applicable to a range of structurally diverse conjugated polymers. In NP photocatalysts composed of a single semiconductor, glycolation suppresses exciton recombination and increases the efficiency of intrinsic charge generation within the NPs, which increases their HER rate compared to NPs composed of their non-glycolated analogues. However, in NPs composed of a single semiconductor, most of these charges decay via geminate recombination on the nanosecond timescale, too fast for efficient hole scavenging by AA, which limits their H_2 evolution efficiency. Fabricating NPs composed of two semiconductors with a type II energy level offset introduces a D/A heterojunction within the NPs that efficiently dissociates excitons at the D/A interface. Glycolation of the donor polymer in these NPs suppresses both geminate and non-geminate recombination. The resultant generation of long-lived charges within the glycolated D/A NPs enables efficient hole scavenging by AA, which greatly enhances their photocatalytic H_2 evolution rate. The effectiveness of glycol side chains in suppressing the ps-ns exciton and charge transfer state recombination losses observed for our neat and D/A NPs herein is remarkable, suggesting an impact of glycolation on the high frequency (GHz) permittivity of our NPs. The effectiveness of glycolation in suppressing such ps-ns recombination in our NPs may be associated with the hydrophilicity and small size of these NPs, facilitating the ingress of highly polar water molecules into these NPs, and thus substantially increasing the effective dielectric response of these NPs on a timescale fast enough to screen the coulomb attraction of excitons and CT states.[50,51]

Methods

Details of the experimental methods can be found in the supporting information.

Supporting Information

Supporting Information is available from the Wiley Online Library or from the author.

Acknowledgements

We acknowledge financial support from KAUST, including Office of Sponsored Research (OSR) awards no. OSR-2018-CRG/CCF-3079, OSR-2019-CRG8-4086 IED-OSR-2019-4454 and OSR-2018-CRG7-3749. We acknowledge funding from ERC Synergy Grant SC2 (610115), the European Union's Horizon 2020 research and innovation programme under grant agreement n°952911, project BOOSTER and grant agreement n°862474, project RoLA-FLEX, as well as EPSRC Project EP/T026219/1. SGC acknowledges European Union's Horizon 2020 research and innovation programme under the Marie Sklodowska-Curie grant agreement No 886664 (PolyNanoCat project).

Received: ((will be filled in by the editorial staff))
Revised: ((will be filled in by the editorial staff))
Published online: ((will be filled in by the editorial staff))

References

[1] Q. Wang, K. Domen, *Chem. Rev.* **2020**, *120*, 919.
[2] J. Schneider, M. Matsuoka, M. Takeuchi, J. Zhang, Y. Horiuchi, M. Anpo, D. W. Bahnemann, *Chem. Rev.* **2014**, *114*, 9919.
[3] M. Ni, M. K. H. Leung, D. Y. C. Leung, K. Sumathy, *Renew. Sustain. Energy Rev.* **2007**, *11*, 401.
[4] P. Yohan, H. Takashi, D. Kazunari, in *Curr. Dev. Photocatal. Photocatalytic Mater.*, Elsevier, **2020**, pp. 141–157.
[5] T. Takata, J. Jiang, Y. Sakata, M. Nakabayashi, N. Shibata, V. Nandal, K. Seki, T. Hisatomi, K. Domen, *Nature* **2020**, *581*, 411.
[6] G. Zhang, L. Lin, G. Li, Y. Zhang, A. Savateev, S. Zafeiratos, X. Wang, M. Antonietti, *Angew. Chemie Int. Ed.* **2018**, *57*, 9372.
[7] S. Yang, Y. Gong, J. Zhang, L. Zhan, L. Ma, Z. Fang, R. Vajtai, X. Wang, P. M. Ajayan, *Adv. Mater.* **2013**, *25*, 2452.
[8] X. Wang, K. Maeda, A. Thomas, K. Takanabe, G. Xin, J. M. Carlsson, K. Domen, M. Antonietti, *Nat. Mater.* **2009**, *8*, 76.
[9] B. A. Pinaud, J. D. Benck, L. C. Seitz, A. J. Forman, Z. Chen, T. G. Deutsch, B. D. James, K. N. Baum, G. N. Baum, S. Ardo, H. Wang, E. Miller, T. F. Jaramillo, *Energy Environ. Sci.* **2013**, *6*, 1983.
[10] S. Yanagida, A. Kabumoto, K. Mizumoto, C. Pac, K. Yoshino, *J. Chem. Soc. Chem. Commun.* **1985**, *0*, 474.
[11] M. Sachs, R. S. Sprick, D. Pearce, S. A. J. Hillman, A. Monti, A. A. Y. Guilbert, N. J. Brownbill, S. Dimitrov, X. Shi, F. Blanc, M. A. Zwijnenburg, J. Nelson, J. R. Durrant, A. I. Cooper, *Nat. Commun.* **2018**, *9*, 4968.
[12] F. Vilela, K. Zhang, M. Antonietti, *Energy Environ. Sci.* **2012**, *5*, 7819.
[13] P. Guiglion, C. Butchosa, M. A. Zwijnenburg, *Macromol. Chem. Phys.* **2016**, *217*, 344.

[14] V. S. Vyas, V. W. Lau, B. V. Lotsch, *Chem. Mater.* **2016**, *28*, 5191.
[15] F. Beuerle, B. Gole, *Angew. Chemie - Int. Ed.* **2018**, *57*, 4850.
[16] T. Banerjee, K. Gottschling, G. Savasci, C. Ochsenfeld, B. V. Lotsch, *ACS Energy Lett.* **2018**, *3*, 400.
[17] X. Feng, X. Ding, D. Jiang, *Chem. Soc. Rev.* **2012**, *41*, 6010.
[18] J. Kosco, F. Moruzzi, B. Willner, I. McCulloch, *Adv. Energy Mater.* **2020**, *10*, 2001935.
[19] Y. Bai, L. Wilbraham, B. J. Slater, M. A. Zwijnenburg, R. S. Sprick, A. I. Cooper, *J. Am. Chem. Soc.* **2019**, *141*, 9063.
[20] D. J. Woods, S. A. J. Hillman, D. Pearce, L. Wilbraham, L. Q. Flagg, W. Duffy, I. McCulloch, J. R. Durrant, A. A. Y. Guilbert, M. A. Zwijnenburg, R. S. Sprick, J. Nelson, A. I. Cooper, *Energy Environ. Sci.* **2020**, *13*, 1843.
[21] J. Kosco, M. Bidwell, H. Cha, T. Martin, C. T. Howells, M. Sachs, D. H. Anjum, S. Gonzalez Lopez, L. Zou, A. Wadsworth, W. Zhang, L. Zhang, J. Tellam, R. Sougrat, F. Laquai, D. M. DeLongchamp, J. R. Durrant, I. McCulloch, *Nat. Mater.* **2020**, *19*, 559.
[22] M. Sachs, H. Cha, J. Kosco, C. M. Aitchison, L. Francàs, S. Corby, C. L. Chiang, A. A. Wilson, R. Godin, A. Fahey-Williams, A. I. Cooper, R. S. Sprick, I. McCulloch, J. R. Durrant, *J. Am. Chem. Soc.* **2020**, *142*, 14574.
[23] X. Wang, L. Chen, S. Y. Chong, M. A. Little, Y. Wu, W.-H. Zhu, R. Clowes, Y. Yan, M. A. Zwijnenburg, R. S. Sprick, A. I. Cooper, *Nat. Chem.* **2018**, *10*, 1180.
[24] Y. Wang, A. Vogel, M. Sachs, R. S. Sprick, L. Wilbraham, S. J. A. Moniz, R. Godin, M. A. Zwijnenburg, J. R. Durrant, A. I. Cooper, J. Tang, *Nat. Energy* **2019**, *4*, 746.
[25] A. Wadsworth, Z. Hamid, J. Kosco, N. Gasparini, I. McCulloch, *Adv. Mater.* **2020**, *32*, 2001763.
[26] A. Liu, L. Gedda, M. Axelsson, M. Pavliuk, K. Edwards, L. Hammarström, H. Tian, *J. Am. Chem. Soc.* **2021**, jacs. 0c12654.
[27] S. Torabi, F. Jahani, I. Van Severen, C. Kanimozhi, S. Patil, R. W. A. Havenith, R. C. Chiechi, L. Lutsen, D. J. M. Vanderzande, T. J. Cleij, J. C. Hummelen, L. J. A. Koster, *Adv. Funct. Mater.* **2015**, *25*, 150.
[28] B. Meng, J. Liu, L. Wang, *Polym. Chem.* **2020**, *11*, 1261.
[29] Z. Hu, Z. Wang, X. Zhang, H. Tang, X. Liu, F. Huang, Y. Cao, *iScience* **2019**, *13*, 33.
[30] N. Cho, C. W. Schlenker, K. M. Knesting, P. Koelsch, H. L. Yip, D. S. Ginger, A. K. Y. Jen, *Adv. Energy Mater.* **2014**, *4*, 1301857.
[31] A. A. Mohapatra, Y. Dong, P. Boregowda, A. Mohanty, A. Sadhanala, X. Jiao, A. Narayan, C. R. McNeill, J. R. Durrant, S. Patil, *J. Phys. Chem. C* **2021**, *125*, 6896.
[32] S. Sami, R. Alessandri, R. Broer, R. W. A. Havenith, *ACS Appl. Mater. Interfaces* **2020**, *12*, 17783.
[33] N. Koizumi, T. Hanai, *J. Phys. Chem.* **1956**, *60*, 1496.
[34] S. Trasatti, *J. Electroanal. Chem. Interfacial Electrochem.* **1986**, *209*, 417.
[35] K. Landfester, *Adv. Mater.* **2001**, *13*, 765.
[36] S. Holliday, R. S. Ashraf, A. Wadsworth, D. Baran, S. A. Yousaf, C. B. Nielsen, C.-H. Tan, S. D. Dimitrov, Z. Shang, N. Gasparini, M. Alamoudi, F. Laquai, C. J. Brabec, A. Salleo, J. R. Durrant, I. McCulloch, *Nat. Commun.* **2016**, *7*, 11585.
[37] T. H. Thomas, D. J. Harkin, A. J. Gillett, V. Lemaur, M. Nikolka, A. Sadhanala, J. M. Richter, J. Armitage, H. Chen, I. McCulloch, S. M. Menke, Y. Olivier, D. Beljonne, H. Sirringhaus, *Nat. Commun.* **2019**, *10*, 2614.
[38] Y. W. Soon, S. Shoaee, R. S. Ashraf, H. Bronstein, B. C. Schroeder, W. Zhang, Z. Fei, M. Heeney, I. McCulloch, J. R. Durrant, *Adv. Funct. Mater.* **2014**, *24*, 1474.
[39] D. Baran, N. Gasparini, A. Wadsworth, C. H. Tan, N. Wehbe, X. Song, Z. Hamid, W. Zhang, M. Neophytou, T. Kirchartz, C. J. Brabec, J. R. Durrant, I. McCulloch, *Nat. Commun.* **2018**, *9*, 2059.

[40] C.-H. Tan, A. Wadsworth, N. Gasparini, S. Wheeler, S. Holliday, R. S. Ashraf, S. D. Dimitrov, D. Baran, I. McCulloch, J. R. Durrant, *J. Phys. Chem. C* **2019**, *123*, 5826.
[41] N. Cho, C. W. Schlenker, K. M. Knesting, P. Koelsch, H.-L. Yip, D. S. Ginger, A. K.-Y. Jen, *Adv. Energy Mater.* **2014**, *4*, 1301857.
[42] G. Zhang, T. M. Clarke, A. J. Mozer, *J. Phys. Chem. C* **2016**, *120*, 7033.
[43] M. Lenes, F. B. Kooistra, J. C. Hummelen, I. Van Severen, L. Lutsen, D. Vanderzande, T. J. Cleij, P. W. M. Blom, *J. Appl. Phys.* **2008**, *104*, 114517.
[44] X. Chen, Z. Zhang, Z. Ding, J. Liu, L. Wang, *Angew. Chemie Int. Ed.* **2016**, *55*, 10376.
[45] J. Brebels, J. V. Manca, L. Lutsen, D. Vanderzande, W. Maes, *J. Mater. Chem. A* **2017**, *5*, 24037.
[46] A. Nistor, G. Stiubianu, C. Racles, M. Cazacu, *Evaluation of the Water Sorption Capacity of Some Polymeric Materials by Dynamic Vapour Sorption*, **2011**.
[47] K. C. Ng, M. Burhan, M. W. Shahzad, A. Bin Ismail, *Sci. Rep.* **2017**, *7*, 1.
[48] M. Moser, T. C. Hidalgo, J. Surgailis, J. Gladisch, S. Ghosh, R. Sheelamanthula, Q. Thiburce, A. Giovannitti, A. Salleo, N. Gasparini, A. Wadsworth, I. Zozoulenko, M. Berggren, E. Stavrinidou, S. Inal, I. McCulloch, *Adv. Mater.* **2020**, *32*, 2002748.
[49] M. Nikolka, I. Nasrallah, B. Rose, M. K. Ravva, K. Broch, A. Sadhanala, D. Harkin, J. Charmet, M. Hurhangee, A. Brown, S. Illig, P. Too, J. Jongman, I. McCulloch, J. L. Bredas, H. Sirringhaus, *Nat. Mater.* **2017**, *16*, 356.
[50] A. Andryieuski, S. M. Kuznetsova, S. V. Zhukovsky, Y. S. Kivshar, A. V. Lavrinenko, *Sci. Rep.* **2015**, *5*, 1.
[51] N. Shinyashiki, S. Sudo, W. Abe, S. Yagihara, *J. Chem. Phys.* **1998**, *109*, 9843.
[52] W. Zhang, J. Smith, S. E. Watkins, R. Gysel, M. McGehee, A. Salleo, J. Kirkpatrick, S. Ashraf, T. Anthopoulos, M. Heeney, I. McCulloch, *J. Am. Chem. Soc.* **2010**, *132*, 11437.
[53] J. Kosco, I. McCulloch, *ACS Energy Lett.* **2018**, *3*, 2846.
[54] R. Hooper, L. J. Lyons, M. K. Mapes, D. Schumacher, D. A. Moline, R. West, *Macromolecules* **2001**, *34*, 931.
[55] L. Dong, S. Shen, H. Lu, S. Jin, J. Zhang, *ACS Sensors* **2019**, *4*, 1222.
[56] M. Qureshi, K. Takanabe, *Chem. Mater.* **2017**, *29*, 158.

ToC entry:

Employing conjugated polymers functionalized with (oligo)ethylene glycol sidechains in NP photocatalysts can greatly enhance their H_2 evolution efficiency. Glycolation facilitates charge generation and suppresses both geminate and non-geminate charge recombination in donor/acceptor nanoparticles. This results in a high yield of photogenerated charges with lifetimes long enough to efficiently drive ascorbic acid oxidation and H_2 evolution.

Jan Kosco, Soranyel Gonzalez-Carrero, Calvyn T. Howells, Weimin Zhang, Maximilian Moser, Rajendar Sheelamanthula, Benjamin Willner, Tania Hidalgo, Hendrik Faber, Balaji Purushothaman, Michael Sachs, Hyojung Cha, Thomas Anthopolous, Sahika Inal, James R. Durrant, Iain McCulloch**

Oligoethylene glycol sidechains increase charge generation in organic semiconductor nanoparticles for enhanced photocatalytic hydrogen evolution

Supporting Information

Oligoethylene glycol sidechains increase charge generation in organic semiconductor nanoparticles for enhanced photocatalytic hydrogen evolution

Jan Kosco, Soranyel Gonzalez-Carrero, Calvyn T. Howells, Weimin Zhang, Maximilian Moser, Rajendar Sheelamanthula, Lingyun Zhao, Benjamin Willner, Tania C. Hidalgo, Hendrik Faber, Balaji Purushothaman, Michael Sachs, Hyojung Cha, Rachid Sougrat, Thomas D. Anthopoulos, Sahika Inal, James R. Durrant, Iain McCulloch**

Experimental

Synthesis

General Procedures

Reagents and solvents were purchased from commercial suppliers, specifically Sigma-Aldrich, FluoroChem, Acros Organics and Sunatech and were used without any further purification. Reactions were conducted in oven-dried flasks and under an inert nitrogen atmosphere. Thin-layer chromatography (TLC) was conducted on Merck Silicagel 60 F254 plates and developed either by irradiation with short (254 nm) or long wavelength (365 nm) UV light or by staining with potassium permanganate. Silica flash column chromatography was carried out on Merck Geduran Silicagel 60 (40-63 μm).

^{1}H and $^{13}C\{^{1}H\}$ nuclear magnetic resonance (NMR) spectroscopy was performed on a Bruker AV-400 UltraShield spectrometer (400 MHz for ^{1}H and 101 MHz for $^{13}C\{^{1}H\}$) at 298 K and using chloroform-*d* ($CDCl_3$) as the solvent unless stated otherwise. Chemical shifts (δ) are reported in parts per million (ppm) downfield from tetramethylsilane (TMS) and are referenced using residual chloroform (δ_H = 7.26 ppm and δ_C = 77.2 ppm) as internal standard. Coupling constants (*J*) are given in Hertz (Hz) and multiplicities are indicated as singlet (s), doublet (d), triplet (t) or multiplet (m).

Gel permeation chromatography (GPC) was conducted using on an Agilent Technologies 1260 Infinity system and a PLgel 10 μm Mixed-B column employing *ortho*-dichlorobenzene at 80 °C as the eluent.

IDTBT[52] and F8BT[53] were synthesized following literature protocols. PTB7-Th was purchased from Ossila and used without further purification.

Synthesis of FgBT

Diethylene glycol monomethyl ether tosylate (1)

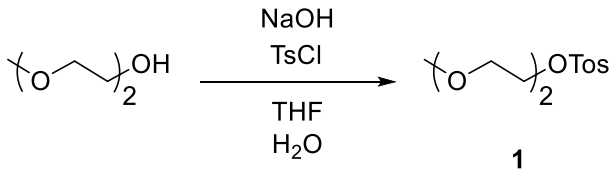

1

Diethylene glycol monomethyl ether (50.0 g, 416 mmol, 1.00 equiv.) was dissolved in 100 mL tetrahydrofuran and cooled to 0 °C. A solution of sodium hydroxide (25.0 g, 625 mmol, 1.50 equiv.) in 100 mL distilled water was added dropwise and the resulting mixture was left to stir for 30 min at 0 °C. Next, a solution of tosyl chloride (83.0 g, 437 mmol, 1.05 equiv.) in 100 mL tetrahydrofuran was added dropwise and the mixture stirred overnight. Distilled water was added, and the aqueous layer was extracted with diethyl ether. The combined organic

phases were washed with water and brine, before being dried over anhydrous sodium sulfate. Excess solvent was removed under reduced pressure. No further purification was required to afford **1** as a clear colorless oil (106 g, 387 mmol, 93% yield).
^{1}H NMR (400 MHz, $CDCl_3$) δ: 7.77 – 7.70 (m, 2H), 7.30 – 7.24 (m, 2H), 4.12 – 4.07 (m, 2H), 3.64 – 3.59 (m, 2H), 3.54 – 3.48 (m, 2H), 3.44 – 3.37 (m, 2H), 3.28 (s, 3H), 2.37 (s, 3H).
The ^{1}H NMR data was consistent with the one reported in literature.[54]

2,7-Dibromo-9,9-bis(2-(2-methoxyethoxy)ethyl)fluorene (2)

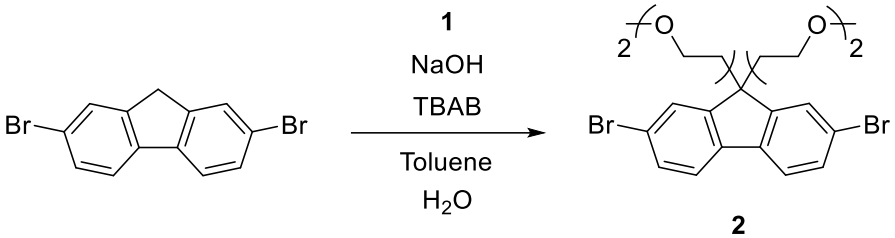

2

2,7-Dibromofluorene (3.50 g, 10.9 mmol, 1.00 equiv.), **1** (8.70 g, 31.7 mmol, 2.90 equiv.) and tetrabutylammonium bromide (0.70 g, 2.2 mmol, 0.20 equiv.) were dissolved in 50 mL toluene and the solution degassed for 20 min. 24 mL of a degassed 1:1 wt/wt solution of sodium hydroxide in water was added to the mixture and the reaction heated to 80 °C overnight. After cooling to room temperature, the reaction was diluted with dichloromethane and the organic layers washed with water and brine before being dried over anhydrous sodium sulfate. Excess solvent was removed under reduced pressure. The crude product was purified by silica flash column chromatography employing a 3:1 v/v mixture of petroleum ether:ethyl acetate as the eluent. **2** was collected as a white solid (4.92 g, 9.35 mmol, 86% yield).
^{1}H NMR (400 MHz, $CDCl_3$) δ: 7.57 (dd, J = 1.7, 0.6 Hz, 2H), 7.53 (dd, J = 8.1, 0.6 Hz, 2H), 7.49 (dd, J = 8.1, 1.7 Hz, 2H), 3.34 – 3.29 (m, 10H), 3.24 – 3.19 (m, 4H), 2.79 (dd, J = 8.1, 6.7 Hz, 4H), 2.39 (dd, J = 8.1, 6.8 Hz, 4H).
^{13}C{^{1}H} NMR (101 MHz, $CDCl_3$) δ: 150.9, 138.4, 130.7, 126.8, 121.7, 121.2, 71.7, 70.0, 66.8, 59.0, 51.9, 39.5.

FgBT

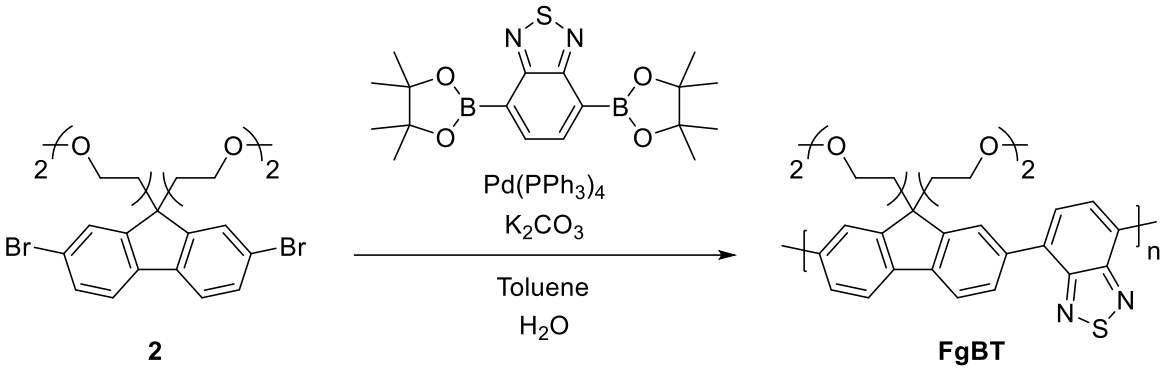

2 **FgBT**

2 (301 mg, 0.572 mmol, 1.00 equiv.), 2,1,3-benzothiadiazole-4,7-bis(boronic acid pinacol ester) (222 mg, 0.572 mmol, 1.00 equiv.) and tetrakis(triphenylphosphine)palladium(0) (12 mg, 0.010 mmol, 0.018 equiv.) were dissolved in 4 mL degassed toluene. To this mixture 1 mL of a degassed 2 M potassium carbonate in water solution was added and the reaction mixture heated to reflux overnight. After cooling to room temperature, the reaction mixture was precipitated into 50 mL of methanol and filtered into a Soxhlet thimble. The crude product was purified by sequential Soxhlet extractions in methanol, acetone, ethyl acetate, hexane and chloroform. Excess solvent of the chloroform fraction was removed under reduced pressure and the product reprecipitated into methanol. **FgBT** was collected by suction filtration and was recovered as an orange powder (260 mg, 91% yield).
GPC (*o*-DCB, 80 °C): M_n = 20.0 kDa, $Đ$ = 1.2.
^{1}H NMR (400 MHz, TCE-d_2) δ: 7.17 (s, 2H), 7.05 (s, 2H), 4.41 (s, 4H), 4.01 (s, 4H), 3.84 (s, 4H), 3.67 (s, 4H), 3.43 (s, 6H).

Tetraethylene glycol monomethyl ether tosylate (3)

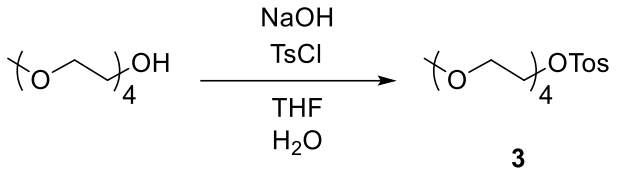

3

Tetraethylene glycol monomethyl ether (25.0 g, 120 mmol, 1.00 equiv.) was dissolved in 30 mL tetrahydrofuran and cooled to 0 °C. A solution of sodium hydroxide (7.20 g, 180 mmol, 1.50 equiv.) in 30 mL distilled water was added dropwise and the resulting mixture was left to stir for 30 min at 0 °C. Next, a solution of tosyl chloride (24.0 g, 126 mmol, 1.05 equiv.) in 30 mL tetrahydrofuran was added dropwise and the mixture stirred overnight. Distilled water was added, and the aqueous layer was extracted with diethyl ether. The combined organic phases were washed with water and brine, before being dried over anhydrous sodium sulfate. Excess solvent was removed under reduced pressure. No further purification was required to afford **3** as a clear colorless oil (35.4 g, 97.7 mmol, 81% yield).
^{1}H NMR (400 MHz, $CDCl_3$) δ: 7.85 – 7.78 (m, 2H), 7.38 – 7.33 (m, 2H), 4.20 – 4.15 (m, 2H), 3.72 – 3.68 (m, 2H), 3.67 – 3.62 (m, 6H), 3.60 (s, 4H), 3.58 – 3.54 (m, 2H), 3.39 (s, 3H), 2.46 (s, 3H).
The ^{1}H NMR data was consistent with the one reported in literature.[55]

1-(Thiophen-2-yl)-2,5,8,11,14-pentaoxapentadecane (4)

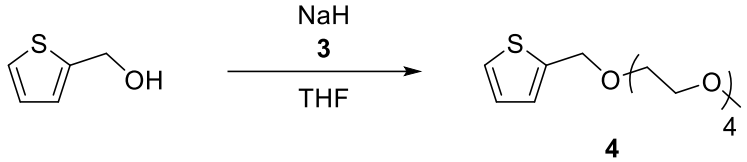

4

A 60% sodium hydride dispersion in mineral oil (2.10 g, 52.6 mmol, 1.32 equiv.) was dissolved in 30 mL anhydrous tetrahydrofuran. To this solution 2-thiophenemethanol (6.00 g, 52.6 mmol, 1.32 equiv.) was added dropwise and the reaction then diluted with 150 mL anhydrous tetrahydrofuran. The reaction was stirred for 30 min then **3** (14.4 g, 39.8 mmol, 1.00 equiv.) was added dropwise. The reaction was stirred overnight. The reaction was quenched by adding water. The aqueous phase was extracted with dichloromethane and the combined organic fractions washed with water and brine before being dried over anhydrous sodium sulfate. Excess solvent was removed under reduced pressure. The crude product was purified by silica flash column chromatography employing a 1:4 v/v mixture of petroleum ether:ethyl acetate as the eluent. **4** was collected as a clear colorless oil (11.0 g, 36.1 mmol, 91% yield).

^{1}H NMR (400 MHz, $CDCl_3$) δ: 7.29 (dd, J = 5.0, 1.3 Hz, 1H), 7.03 – 7.00 (m, 1H), 6.98 (dd, J = 5.0, 3.5 Hz, 1H), 4.74 (d, J = 0.8 Hz, 2H), 3.69 – 3.66 (m, 14H), 3.59 – 3.52 (m, 2H), 3.39 (s, 3H).

Synthesis of gIDTBT

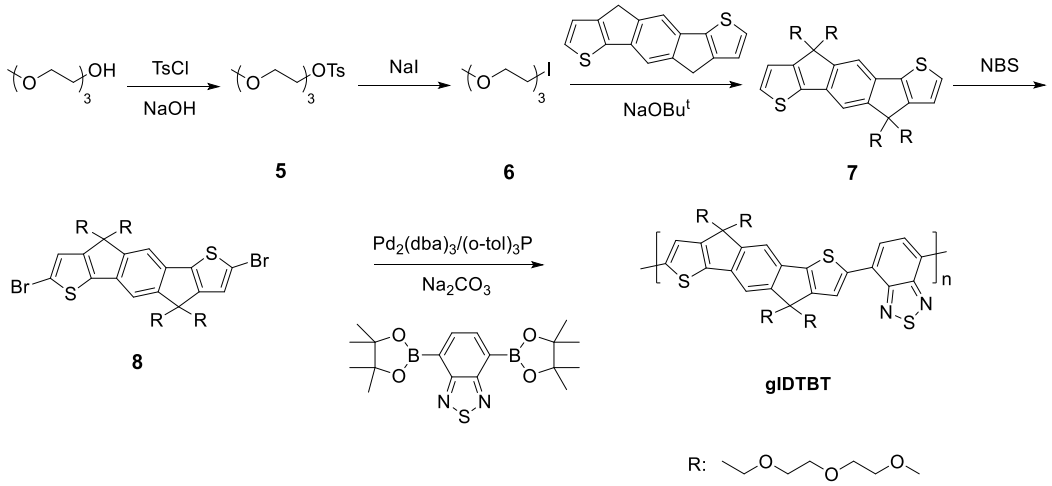

2-(2-(2-Methoxyethoxy)ethoxy)ethyl 4-methylbenzenesulfonate 5

An aqueous solution of sodium hydroxide (5.0 M, 10 mL, 1.57 equiv.) was added dropwise to a solution of 2-(2-(2-methoxyethoxy)ethoxy)ethan-1-ol (5.00 g, 30.5 mmol) in tetrahydrofuran (10 mL) at 0 °C. The reaction mixture was then charged with a solution of p-toluenesulfonyl chloride (6.17 g, 32.4 mmol) in THF (10 mL) and stirred for 4 h at 0° C and for a further 18 h at room temperature. Once complete, the reaction mixture was diluted with distilled water (20 mL) and the aqueous layer extracted into diethyl ether (3 × 25 mL). The combined organic phases were washed with distilled water and brine before being dried over magnesium sulphate. The solvent was removed under reduced pressure. No further purification was required to afford 5 as a clear colourless oil (9.25 g, 97.0 %). 1H NMR (400 MHz, CDCl3): δ 7.79 (d, J = 8.2 Hz, 2H), 7.33 (d, J = 8.0 Hz, 2H), 4.15 (td, J = 4.8, 1.4 Hz, 2H), 3.68 (td, J = 4.8, 1.5 Hz, 2H), 3.63 – 3.56 (m, 6H), 3.56 – 3.50 (m, 2H), 3.36 (s, 3H), 2.44 (s, 3H). 13C NMR (101 MHz, CDCl3): δ 144.85, 133.06, 129.88, 128.01, 71.95, 70.78, 70.59, 69.32, 68.71, 59.06, 21.69.

1-Iodo-2-(2-(2-methoxyethoxy)ethoxy)ethane 6

Compound 5 (8.96 g, 28.3 mmol) and sodium iodide (6.35 g, 42.4 mmol) were dissolved in acetone (65 mL) and the resulting solution was heated to reflux overnight. Once the reaction was complete the reaction mixture was filtered and concentrated in vacuo. The resulting solution was extracted three times into dichloromethane (3 × 25 mL), washed with water and brine and then dried over magnesium sulphate. The solvent was removed under reduced pressure. No further purification was required to afford 6 as a pale red oil (7.44 g, 96.0 % yield). 1H NMR (400 MHz, CDCl3): δ 3.78 – 3.72 (m, 2H), 3.70 – 3.61 (m, 6H), 3.57 – 3.52 (m, 2H), 3.37 (s, 3H), 3.29 – 3.21 (m, 2H); 13C NMR (101 MHz, CDCl3) δ 72.09, 72.04, 70.72, 70.32, 59.17, 3.01.

4,4,9,9-Tetrakis(2-(2-(2-methoxyethoxy)ethoxy)ethyl)-4,9-dihydro-s-indaceno[1,2-b:5,6-b']dithiophene 7

Sodium tert-butoxide (0.567 g, 5.90 mmol) was added portion wise to a solution of 4,9-dihydro-s-indaceno[1,2-b:5,6-b']-dithiophene (0.261 g, 0.983 mmol) in anhydrous dimethylformamide (10 mL). The resulting mixture was heated for 1.5 h at 80 °C, then 6 (1.364 g, 4.978 mmol) was added dropwise. Following complete addition, the reaction mixture was heated overnight at 80 °C. Once complete, the reaction mixture was quenched by pouring into ice-water. The resulting solution was extracted three times into ethyl acetate (3 × 25 mL) and washed with water and brine before being dried over magnesium sulphate. The solvent was removed under reduced pressure to give a dark brown solid. The latter was purified by flash column chromatography on silica using a 1:20 v/v methanol:ethyl acetate mixture as eluent to afford 7 as an off-white solid (0.456 g, 0.536 mmol, 46.4 % yield): 1H NMR (400 MHz, CDCl3) δ 7.33 (s, 2H), 7.28 (d, J = 4.8 Hz, 2H), 7.00 (d, J = 4.9 Hz, 2H), 3.57 – 3.51 (m, 8H), 3.51 – 3.44 (m, 16H), 3.33 (s, 12H), 3.31 – 3.26 (m, 8H), 3.05 – 2.83 (m, 8H), 2.45 – 2.22 (m, 8H). 13C NMR (101 MHz, CDCl3) δ 153.58, 152.10, 141.49, 135.43, 127.34, 121.79, 113.75, 72.00, 70.63, 70.59, 70.21, 67.50, 59.12, 49.80, 38.74; MS (MALDI-ToF): m/z calculated for C44H66O12S2: 850.40; m/z found 851.6 (M + H)+.

2,7-Dibromo-4,4,9,9-tetrakis(2-(2-(2-methoxyethoxy)ethoxy)ethyl)-4,9-dihydro-s-indaceno[1,2-b:5,6-b']dithiophene 8

Compound 7 (0.456 g, 0.536 mmol) and N-Bromosuccinimide (0.229 g, 1.24 mmol) were dissolved in a 2:1 v/v anhydrous tetrahydrofuran:anhydrous dimethylformamide solution (20 mL) and stirred for 30 min in the dark. Following quenching by addition of water (20 mL), the reaction mixture was extracted three times into ethyl acetate (3 × 25 mL). The combined organic layers were then washed with water and brine before being dried over magnesium sulphate. The solvent was removed under reduced pressure. No further purification was required to afford 8 as an off-white solid (0.476 g, 0.473 mmol, 88.3 % yield): 1H NMR (400 MHz, CDCl3) δ 7.23 (s, 2H), 7.04 (s, 2H), 3.57 – 3.53 (m, 8H), 3.51 – 3.43 (m, 16H), 3.33 (s, 12H), 3.30 – 3.27 (m, 8H), 2.94 – 2.88 (m, 8H), 2.38 – 2.18 (m, 8H). 13C NMR (101 MHz, CDCl3) δ 152.81, 151.17, 141.55, 135.27, 125.22, 113.66, 113.45, 71.98, 70.61, 70.60, 70.25, 67.33, 59.10, 50.91, 38.52. MS (MALDI-ToF): m/z calculated for C44H64Br2O12S2: 1006.22; m/z found 1007.3 (M + H)+.

gIDTBT

A mixture of diboromide 8 (0.43 g, 0.43 mmol), 2,1,3-benzothiadiazole-4,7-bis(boronic acid pinacol ester) (0.17 g, 0.43 mmol), $Pd_2(dba)_3$ (8.0 mg, 8.7×10^{-3} mmol), $(o\text{-}tol)_3P$ (10.6 mg, 0.035 mmol), Na_2CO_3 (1.0 M, 1 ml) and Alioquat 336 (0.5 ml) in toluene (20 ml) was degassed with argon for 20 min, then stirred overnight at 110 ^oC. After cooled to room temperature, the reaction mixture was poured into methanol, and the precipitate was collected in a thimble. Soxhlet extraction was carried out with methanol, acetone, hexane, and chloroform where the polymer dissolved in chloroform. The solvent was removed under reduced pressure and the polymer was precipitated in ethyl acetate, followed by the addition of hexane at 0 °C. After filtration, the polymer was dried under vacuum to give product as a dark blue solid (0.29 g, 70%). 1H NMR (400 MHz, CDCl3): δ 8.14 – 8.39 (br, 2H), 7.92-8.10

(br, 2H), 7.45-7.59 (br, 4H), 3.45-3.64 (br, 24H), 3.37 (br, 20H), 2.87-3.24 (br, 8H), 2.21-2.73 (br, 8H). GPC(CHCl3, RI): Da Mn 18 × 103 and Mw 28 × 103.

Synthesis of gPTB7-Th

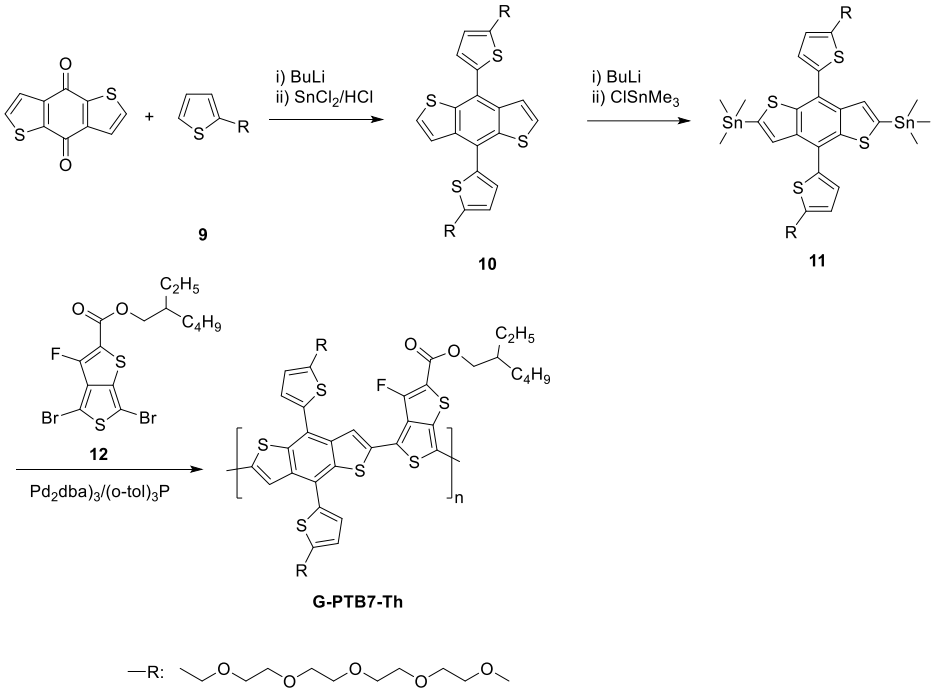

4,8-Bis(5-(2,5,8,11,14-pentaoxapentadecyl)thiophen-2-yl)benzo[1,2-b:4,5-b']dithiophene 9

Compound **9** (2.50 g, 8.22 mmol, 4.00 equiv.) was dissolved in 40 mL anhydrous tetrahydrofuran and the resulting solution cooled to 0 °C. A *n*-BuLi solution in hexanes (2.5 M, 3.3 mL, 8.3 mmol, 4.0 equiv.) was subsequently added dropwise. The reaction was heated to 50 °C and stirred for 1 h. Benzo[1,2-b:4,5-b′]dithiophene-4,8-dione (0.45 g, 2.1 mmol, 1.0 equiv.) was added in one portion and the reaction stirred for an additional 1 h. Following cooling to room temperature, a solution of tin(II) chloride dihydrate (3.71 g, 16.4 mmol, 4.00 equiv.) in 8 mL 10% hydrochloric acid was added dropwise and the reaction stirred for an additional 1.5 h. Following completion, the reaction was poured into water and the aqueous phase extracted with diethyl ether. The combined organic layers were washed with water and brine before being dried over anhydrous sodium sulfate. Excess solvent was removed under reduced pressure. The crude product was purified by silica flash column chromatography employing a 4:1 v/v mixture of dichloromethane:acetone as the eluent. **10** was collected as a pale-yellow oil (0.77 g, 47%). ^{1}H NMR (400 MHz, $CDCl_3$) δ: 7.64 (d, J = 5.6 Hz, 2H), 7.49 (d, J = 5.7 Hz, 2H), 7.37 (d, J = 3.5 Hz, 2H), 7.16 (dt, J = 3.6, 0.8 Hz, 2H), 4.85 (d, J = 0.8 Hz, 4H), 3.82 – 3.63 (m, 28H), 3.59 – 3.53 (m, 4H), 3.39 (s, 6H).

G-PTB-Th

Compound **10** (0.42 g, 0.57 mmol) was dissolved in anhydrous THF (10 mL) and cooled down to -78°C, followed by the addition of n-butyl lithium (1.6 M in hexanes, 1.10 ml, 1.76 mmol) dropwise, and the mixture was stirred for 1 hour at -78 °C. A solution of trimethyltinchloride in hexanes (2.0 mL, 2.0 mmol) was subsequently added, the mixture was allowed to warm up to room temperature and stirred for 1 hour. The solvent was evaporated affording **11** which was used for the next step without further purification. A mixture of **11** (0.17 g, 0.16 mmol), **12** (75.6 mg, 0.16 mmol), $Pd_2(dba)_3$ (5.1 mg, 5.6×10^{-3} mmol), $(o\text{-}tol)_3P$ (6.4 mg, 0.021 mmol), in chlorobenzene (5 ml) was degassed with argon for 10 min, then stirred overnight at 120 °C. After cooled to room temperature, the reaction mixture was poured into methanol, and the precipitate was collected in a thimble. Soxhlet extraction was carried out with methanol, acetone, hexane, and chloroform where the polymer dissolved in chloroform. The solvent was removed under reduced pressure and the polymer was precipitated in hexane. After filtration, the polymer was dried under vacuum to give product as a dark purple solid (97.6 mg, 55%). GPC ($CHCl_3$, RI): Mn 9×10^3 g/mol and Mw 17×10^3 g/mol.

Transient absorption spectroscopy (TAS)

Ultrafast TAS analysis of neat and D/A NPs dispersed in water were carried out by using a amplified Ti:sapphire laser (Solstice, Spectra Physics), with a 800 nm laser pulse (92 fs, 1 kHz repetition rate). The pump laser at 650 nm excitation wavelength is generated through an optical parametric amplifier (TOPAS Prime, Light Conversion) and a frequency mixer (NirUVis, Light Conversion). The probe pulse at specific time delay is generated through a delay stage, which delay it by an adjustable period (maximum of 6 ns) relative to pump pulse. The probe light continuum in the visible (450−800 nm) or NIR (850−1400 nm) region is generated by focusing the probe pulse into a sapphire crystal. Then, the probe pulse is divided before the sample into two pulses, one is directed to the sample and the other is used as a reference. Both pulses are directed to separated multichannel spectrometer (Si or InGaAs sensor). The continuum probe pulse on the samples is spatially overlapped with the pump pulse. Every other pump pulse was chopped by a synchronized chopper such that the ground state and excited state of the sample are probed in an alternating manner, and the absorbance difference is calculated from these two signals. Pulse energies were measured using an energy meter (OPHIR Photonics, VEGA P/N 7Z01560), using a 500 μm diameter aperture. All suspensions were prepared to absorb an equal number of photons (absorbance of 0.5 at the excitation wavelength) in 5 mm quartz cuvettes (Hellma Analytics) and measured in Argon atmosphere.
The deconvoluted transient kinetics for the exciton and polaron of gIDTBT NPs probed in the NIR were determined with spectral models for these two species using a custom global analysis code. To this end, the transient spectrum probed at 0.5 ps after excitation was used as a spectral model for the exciton as the transient signal at that time arises primarily from the excited states absorption of gIDTBT excitons (broad positive band at 1300 nm). In the same way, the transient spectrum at 1000 ps was used as a spectral model for the gIDTBT polaron. Microsecond−Second TAS was carried out by using a Nd:YAG laser (OPOTEK Opolette 355 II, 6 ns pulse width), which generates visible/NIR pulses (410−2200 nm). The probe beam is generated from a quartz halogen lamp (100 W) and sequentially directed through the sample, a monochromator and finally onto a Si photodiode detector (Hamamatsu S1722-01). Pump pulses are directed to the sample through a liquid light guide and are overlapped with the probe beam at the position of the sample. Data acquisitions are triggered by scattered laser light using a photodiode. Appropriate long pass filters were positioned before the sample and between the sample and the detector to attenuate scattered laser light. A home-built LabVIEW-based software package was used to acquire the data on two different time scales simultaneously: the microsecond−millisecond signal is sampled using an oscilloscope (Tektronix DPO 3012) after amplification (Costronics 2011 amplifier), whereas the millisecond−second signal is sampled without amplification using a DAQ card (National Instruments USB-6361). Pulse energies were measured using an energy meter (OPHIR Photonics, VEGA P/N 7Z01560). All suspensions were prepared at equal numbers of absorbed photons (absorbance of 0.5 at the excitation wavelength) in 5 mm quartz cuvettes (Hellma Analytics) and measured in Argon atmosphere.

Nanoparticle fabrication:
Individual stock solutions (0.50 mg/mL) of the donor polymers and small molecule acceptors were prepared in chloroform. The solutions were heated overnight (80 °C) to ensure complete dissolution and filtered (0.2 um PTFE). Nanoparticle precursor solutions were prepared from the stock solutions by mixing them in the ratio of the desired nanoparticle composition. For example, to fabricate nanoparticles composed of a 1:1 blend of gIDTBT:oIDTBR by mass, 2.5 mL of the gIDTBT stock solution (0.5 mg/mL) was added to 2.5 mL of the oIDTBR stock solution (0.5 mg/mL) to form 5 mL of nanoparticle precursor solution containing 1.25 mg of

gIDTBT and 1.25 mg of oIDTBR. 5 mL of the nanoparticle precursor solution was then added to a 0.5 wt.% solution of sodium dodecyl sulfate (SDS) in water (10 mL), and stirred vigorously for 15 min at 40 °C to form a pre-emulsion, which was then sonicated for 5 min with an ultrasonic processor (Sonics VibraCell VCX130PB) to form a mini-emulsion. The mini-emulsion was heated at 85 °C under a stream of air to remove the chloroform, leaving a surfactant stabilised nanoparticle dispersion in water. The total volume of the nanoparticle dispersion was adjusted to 7.5 mL with MilliQ water. 3 mL of the nanoparticle dispersion (containing 1 mg of NPs) was used for each H_2 evolution experiment.

DLS:

The size distribution of each nanoparticle batch was measured by dynamic light scattering (DLS, Malvern Zetasizer ZS, **Fig. S1**, **Tables S1-S3**). **Fig. S1** shows that all NP batches had unimodal size distributions and that the Z_{avg} hydrodynamic diameter within each series remained relatively constant. This is important when comparing HER rates between nanoparticles with different compositions because NP size affects the total available surface area, which may affect the HER rate. Having samples with similar size distributions minimises this variation and allows the effects of nanoparticle composition and morphology to be isolated.

TEM:

Cryo Transmission Electron Microscopy (cryoTEM) of the samples was carried out with a Titan Krios 80-300 TEM from Thermo-Fisher Scientific, USA. This microscope is optimized for carrying out cryoTEM analysis of liquid samples. It is also equipped with an energy-filter of model GIF Quantum 968 from Gatan, Inc., USA, underneath the column to filter the energy-loss electrons to improve the contrast in the acquired images. Moreover, behind the GIF column, a highly sensitive direct electron complementary metal oxide semiconductor (CMOS) camera of model K2, also from Gatan, Inc., USA, was installed for the recording of high-resolution images at extremely low electron dose conditions (~1 e/Å2). Specimen preparation of samples for cryoTEM analysis was carried out by using an automated plunge-freezing tool of model Vitrobot Mark-IV. Moreover, the specimens were prepared with a special type of copper TEM-grid of model Quatifoil MultiA. These grids have a carbon layer with various size holes and were chosen with a purpose of varying ice-thickness in the holes. In this way, the chance of organic particles being present in the specimen was dramatically higher than with the single hole-size carbon containing grid. Each specimen was prepared by placing 3.5 micro-litre of solution onto grids followed by 1 second of blotting-time and plunge-freezing into liquid ethane cryogen. The cryoTEM analysis was performed by setting the microscope at the accelerating voltage of 300 kV. Prior to the analysis, the microscope as well as GIF were aligned to have higher quality images. Furthermore, the images were recorded under so called dose-fractionation conditions. In fact, instead of acquiring a single frame with total electron beam exposure time, the images were acquired in stacks that contained frames whose exposure time was more than ten times smaller than the total exposure time. The acquired stacks were then aligned and summed along z-direction in order to have final images. This exercise of image-recording ensured higher quality images of organic particles with as minimum damage as possible. The total electron dose given to images, acquired at low-magnifications (<50,000X) was kept below 10 e/Å^2. Whereas, higher magnification images (>100,000X) received the electron dose of about 20 e/Å^2 so as to maintain a good signal-to-noise condition. It is to be noted that the entire image acquisition as well as processing was performed using Gatan Microscopy Suite of version 3.2.

Hydrogen evolution:

Hydrogen evolution was measured using ascorbic acid (AA) as a sacrificial electron donor. Nanoparticles (1 mg) in 0.2 M AA (12 mL) were loaded into a recirculating batch reactor (illumination area = 4.41 cm^2) which has been previously reported.[56] The desired Pt loading was achieved by adding a specific amount of aqueous potassium hexachloroplatinate solution

(0.401 mg/mL Pt). The reactor was evacuated and purged with Ar 5 times to remove oxygen, and the pressure was set to 100 Torr. The suspension was stirred and illuminated with a solar simulator (Asahi Max 303) fitted with a UV-IR mirror module and an AM1.5g filter. The light intensity was adjusted to 100 $mWcm^{-2}$ (1 sun) before each experiment using a calibrated reference solar cell (Newport 91150V) and H_2 evolution was quantified by a gas chromatograph equipped with a thermal conductivity detector.

Nanoparticle recycling:

After each 24 h cycle of the extended stability test (Figure 2c) the NPs were removed from the reaction solution using a centrifugal filter (Millipore Amicon Ultra – 15 30,000 NMWL cellulose membrane). The NPs were loaded into the centrifugal filter and centrifuged at 2000 rcf for 10 min. After centrifugation, 1.5 mL of NP suspension was retained inside the filter and a clear filtrate remained in the centrifuge tube. The volume of the NP suspension was adjusted to 3 mL with 0.5wt.% SDS solution in MilliQ water, and H_2 evolution was measured as described above using fresh AA. No further Pt was added.

EQE measurements:

EQE measurements were carried out in the same way as hydrogen evolution measurements, but with suitable band pass filters fitted to the light source. The sample was first illuminated under simulated solar light for 3 h to complete Pt photodeposition. Then the reactor was evacuated and purged with Ar 5 times to remove all the H_2 evolved during this time. The light source was fitted with a band pass filter, and the photocatalyst was illuminated with filtered light within a narrow wavelength range. The EQE was calculated using **Equation 1**, where nH_2 represents the number of moles of H_2 evolved per hour, and n photons represents the total number of photons incident on the sample surface (Illumination area = 4.41 cm^2) per hour. Photon flux was measured using a calibrated spectrometer (Ocean Optics USB2000 calibrated with an Ocean Optics DH3-plus light source) fitted with a fibre optic cable and a 0.4778 cm^2 cosine corrector.

Equation 1:

$$EQE\ (\%) = \frac{200n\ H_2}{n\ photons}$$

Dynamic water vapour adsorption (DVS)

DVS analysis (Hidden Isochema IGAsorp) was carried out on dry polymer powders.

Contact angle measurements

Contact angle measurements (Kruss DSA 100B) were taken on thin polymer films spin coated on polyethylene naphthalate substrates.

Quartz Crystal Microbalance with Dissipation monitoring (QCM-D)

QCM-D measurements were performed with a Q-sense analyser (QE401, Biolin Scientific), using SiO_2-coated crystal sensors. The QCM-D response of bare sensors was monitored in air, water and L-ascorbic acid 0.2 M. Fluid injection into the chamber causes large changes in the QCM-D signals, which must be excluded from the mass uptake calculations. IDT-BT and gIDT-BT were dissolved in chloroform at a concentration of 10 mg/mL and spin-coated onto previously measured clean crystal sensors. As done with bare sensors, polymer-coated sensors were monitored in the three different environments. We compare the absolute difference among several overtones between the bare and the coated sensors using the “Stitch data” function of the Q-Soft software. Mass uptake was calculated using the Sauerbrey equation, which relates the changes in mass (Δm) to the frequency differences (Δf), using one overtone (n) as shown in equation. (1),

$$\Delta_m = \frac{-17.7}{n} \Delta f_n \quad (1)$$

or by approximating the films as Kelvin-Voigt elements, with both viscous and elastic properties. Viscoelastic Kelvin-Voigt elements have a complex shear modulus defined as:

$$G^* = \mu + i2\pi f\eta \quad (2)$$

where G* is the complex shear modulus, μ is elasticity (kg m^{-1} s^{-2}), η is viscosity (kg m^{-1} s^{-1}) and f is the frequency. Mass of a viscoelastic film was calculated by fitting at least three overtones of f and D and estimating the complex shear modulus using the software QTools.

Atomic Force Microscopy (AFM)

AFM measurements were performed in tapping mode, using a Veeco Dimension Icon SPM equipment and Bruker AFM probes with spring constant k = 200 N/m. The measurements were performed with polymer films which were spin-coated on polyethylene naphthalate

substrates to prevent delamination upon fluid exposure. A portion of the films were removed to obtain an overhang for thickness measurements. After the dry films were imaged, they were submerged in water overnight and imaged again after removing excess water.

Supplementary figures

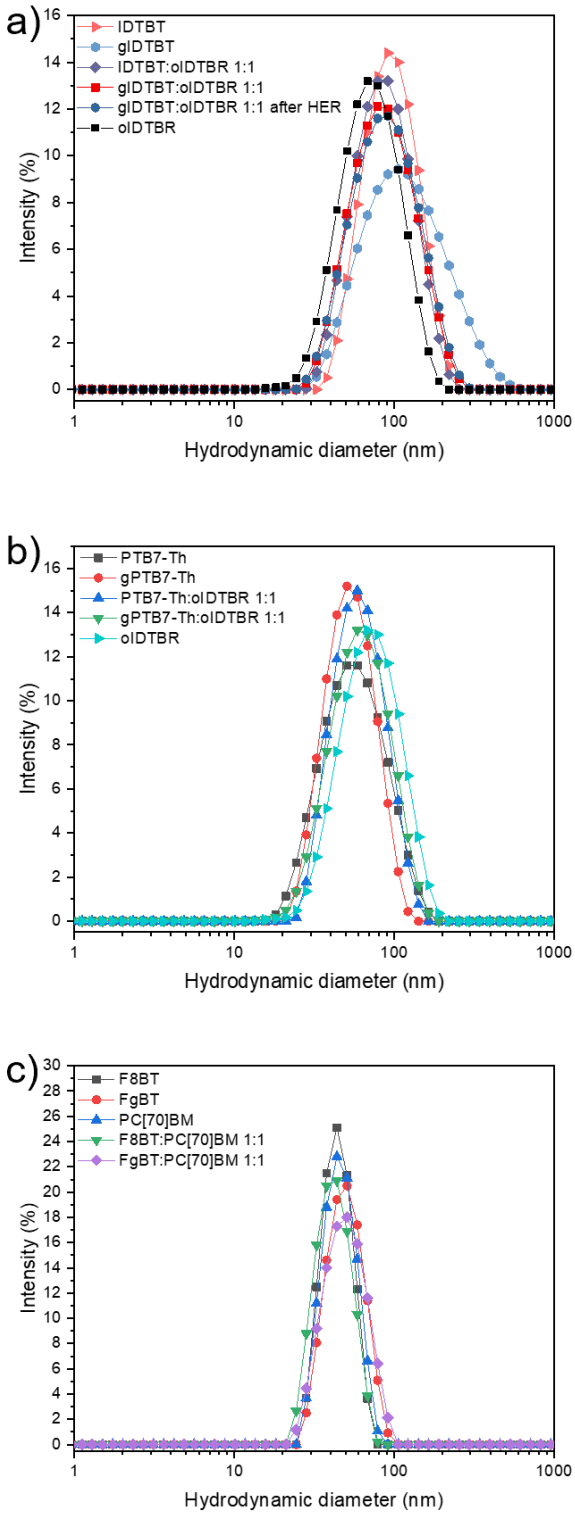

Figure S1: Nanoparticle (NP) size distributions of a) NPs composed of IDTBT, gIDTBT, oIDTBR b) NPs composed of PTB7-Th, gPTB7-Th, oIDTBR c) NPs composed of F8BT, FgBT, PC[70]BM measured by dynamic light scattering (DLS). Note: histograms have been plotted as frequency polygons for greater clarity.

Table S1: DLS size distribution parameters of nanoparticles (NPs) composed of IDTBT, gIDTBT, oIDTBR.

Sample	**Z-Average diameter (nm)**	**Dispersity**
IDTBT	85.03	0.155
gIDTBT	101.6	0.255
oIDTBR	63.53	0.603
IDTBT:oIDTBR (1:1)	70.43	0.228
gIDTBT:oIDTBR (1:1)	68.96	0.259
g-lDTBT:oIDTBR (1:1) + 10% Pt after 16h HER	71.78	0.238

Table S2: DLS size distribution parameters of nanoparticles (NPs) composed of PTB7-Th, gPTB7-Th, oIDTBR.

Sample	**Z-Average diameter (nm)**	**Dispersity**
PTB7-Th	55.75	0.278
gPTB7-Th:oIDTBR 1:1	55.81	0.138
PTB7-Th:oIDTBR 1:1	56.32	0.108
gPTB7-Th	57.41	0.3
oIDTBR	63.53	0.255

Table S3: DLS size distribution parameters of nanoparticles (NPs) composed of F8BT. FgBT, PC[70]BM.

Sample	**Z-Average diameter (nm)**	**Dispersity**
F8BT	70.03	0.216
FgBT	54.66	0.227
PC[70]BM	64.73	0.162
FgBT:PC[70]BM 1:1	53.84	0.253
F8BT:PC[70]BM 1:1	61.99	0.275

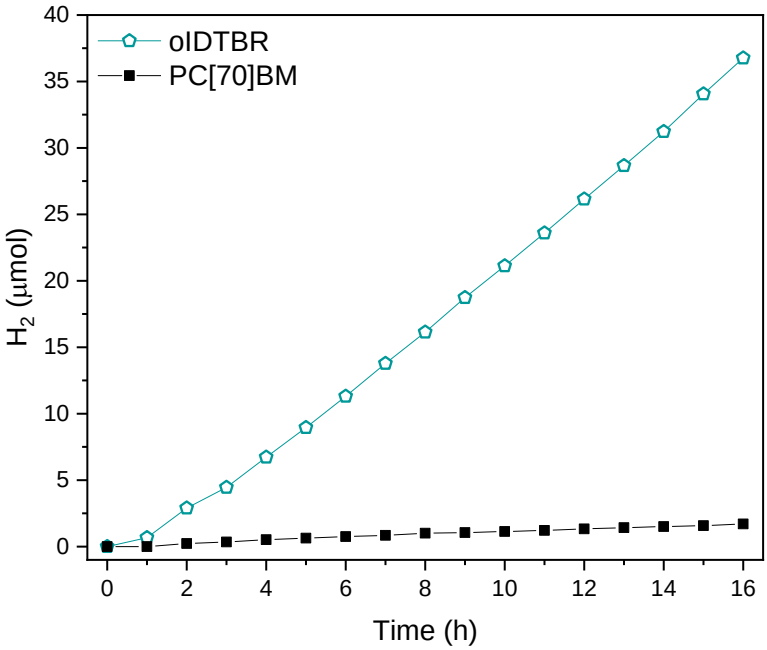

Figure S2: H_2 evolution vs. time of NPs composed of oIDTBR and $PC_{71}BM$. H_2 evolution conditions: 1 mg nanoparticles, 0.2 mol l^{-1} ascorbic acid (12 ml), pH 2, 10 µg (10 wt.%) Pt, AM1.5g solar simulator at 100 $mWcm^{-2}$ (1 sun), 4.41 cm^2 illumination area. Data presented are the average of 3 repeat runs.

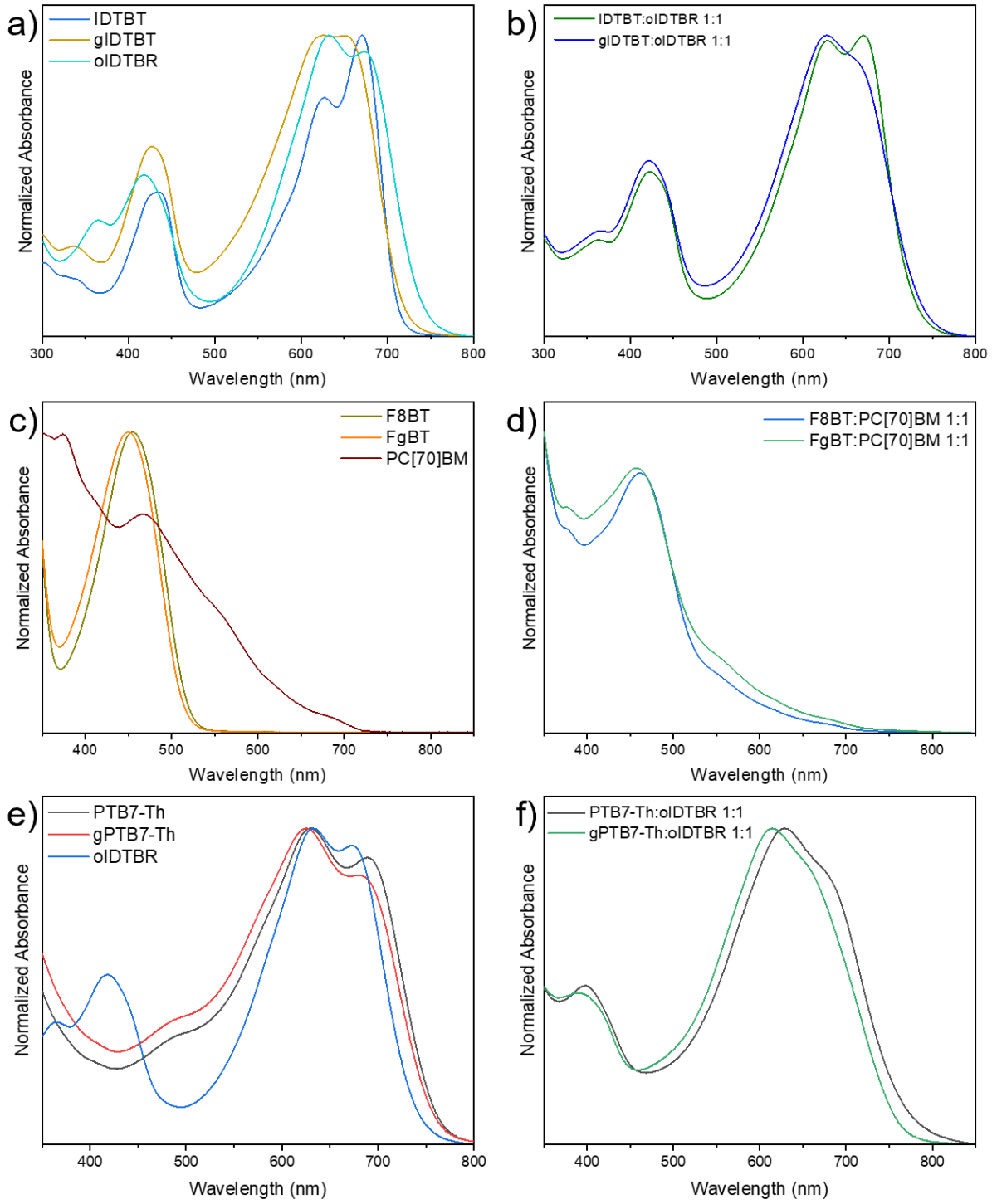

Figure S3: Normalized UV-Visible absorption spectra of nanoparticle dispersions composed of a), c), e) Individual semiconductors, and b), d), f) their blends.

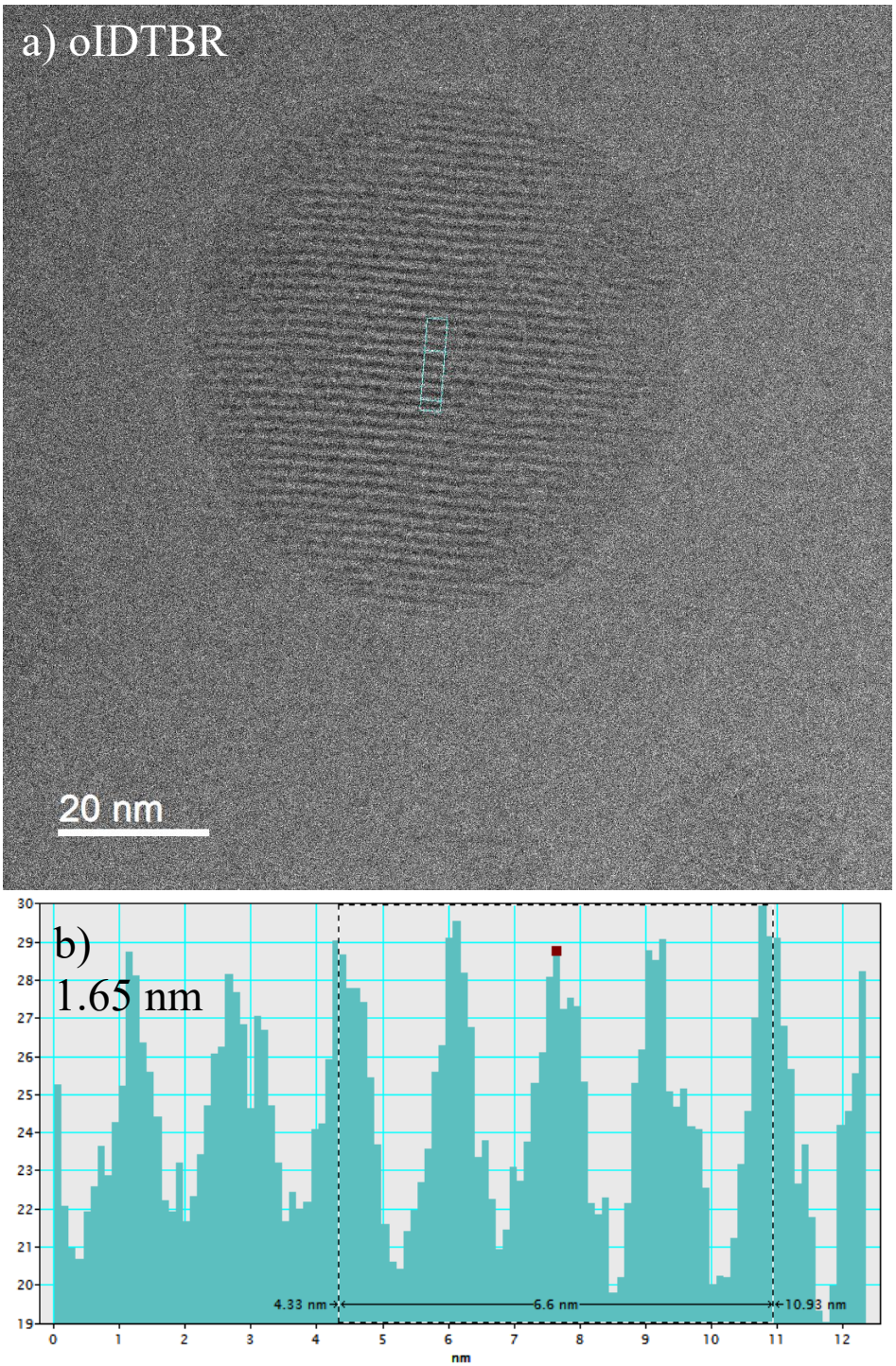

Figure S4: a) Bright field cryo TEM image of an oIDTBR nanoparticle. b) Profile of the periodic spacing (1.65 nm) highlighted in the rectangle in a).

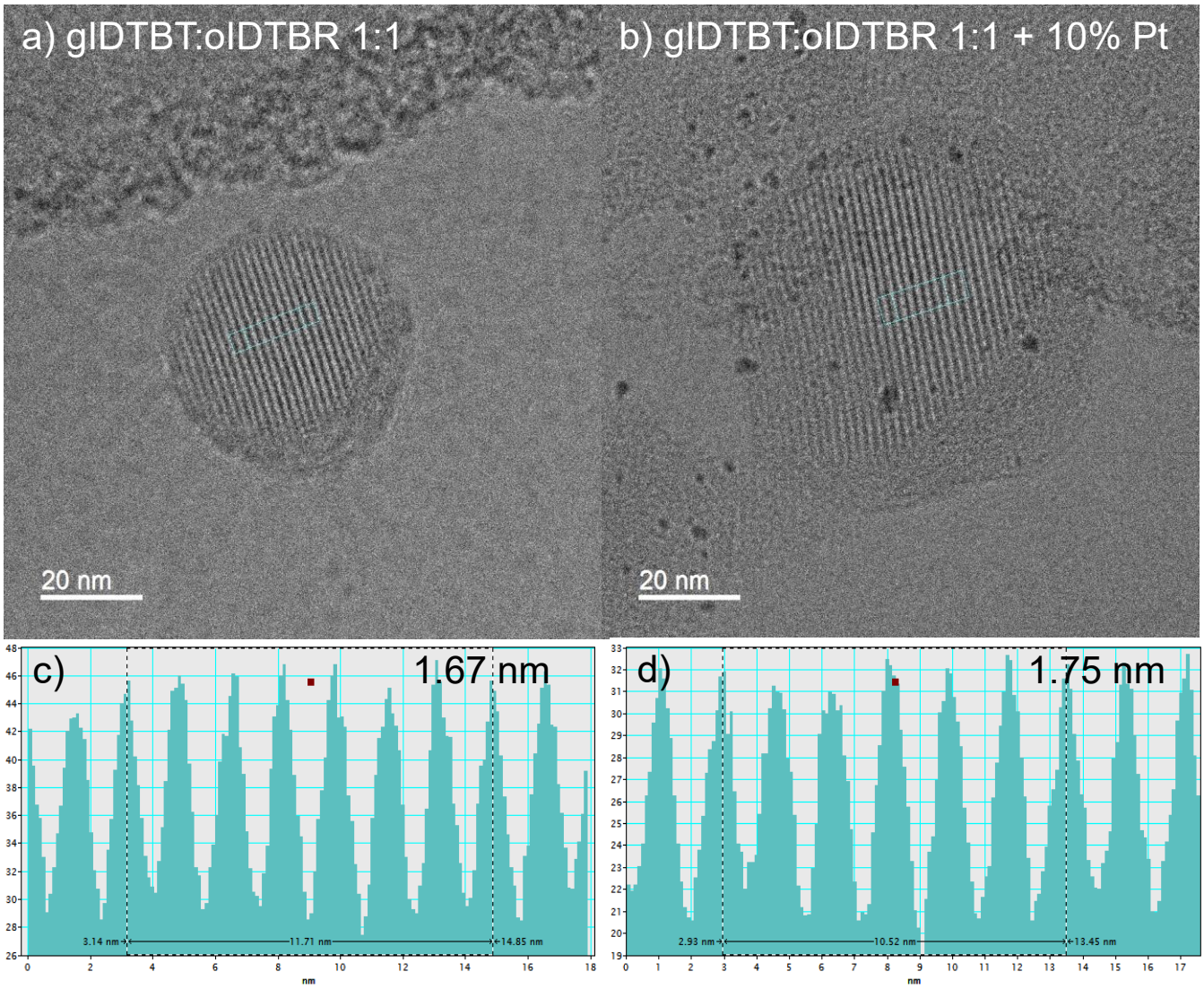

Figure S5: Bright field cryo TEM images of **a)** a nanoparticle composed of a 1:1 gIDTBT:oIDTBR blend. **b)** a nanoparticle composed of a 1:1 gIDTBT:oIDTBR blend after the deposition of 10 wt.% Pt and 20 h H_2 evolution. Images **c)** and **d)** display profiles of the periodic spacings highlighted in the rectangles in images a) and b) respectively.

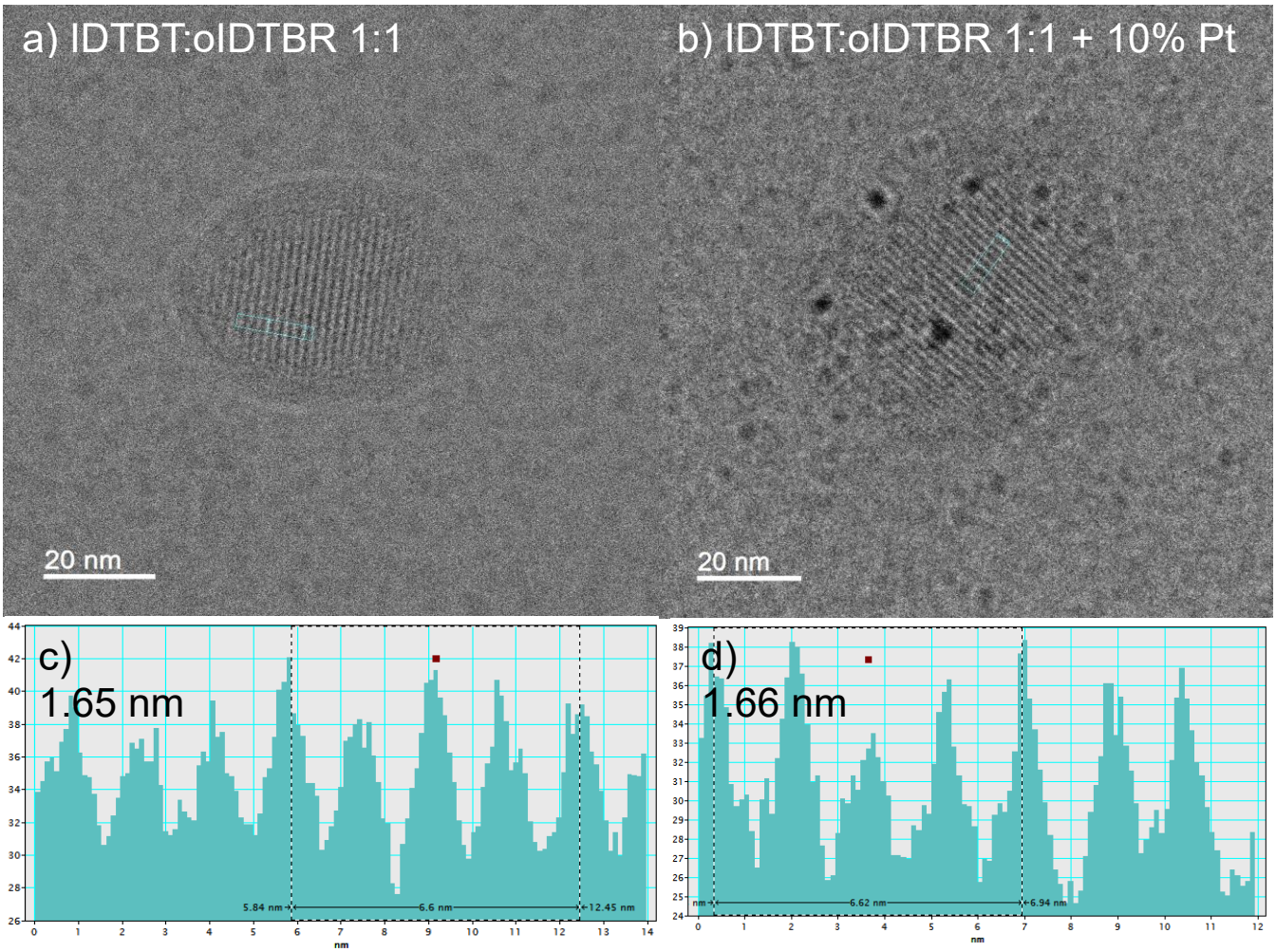

Figure S6: Bright field cryo TEM images of **a)** a nanoparticle composed of a 1:1 IDTBT:oIDTBR blend. **b)** a nanoparticle composed of a 1:1 IDTBT:oIDTBR blend after the deposition of 10 wt.% Pt and 20 h H_2 evolution. Images **c)** and **d)** display profiles of the periodic spacings highlighted in the rectangles in images a) and b) respectively.

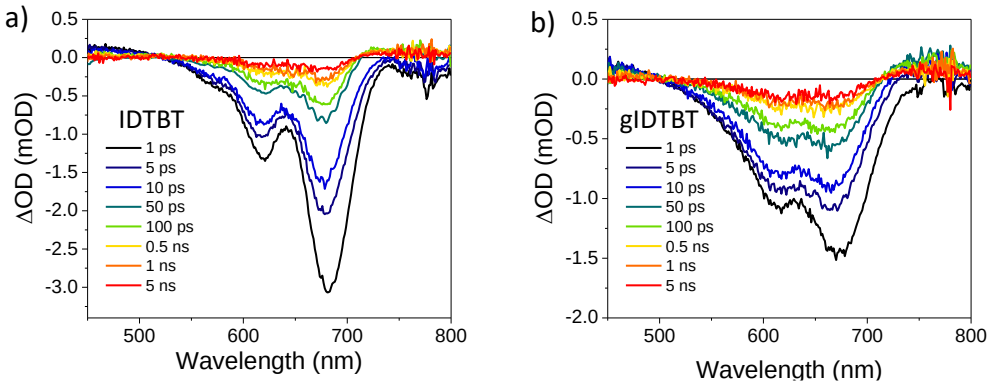

Figure S7. Ultrafast transient absorption spectra of a) IDTBT and b) gIDTBT NPs at different delay times, excited at 650 nm (5 μJ cm^{-2}) and probed in the visible region.

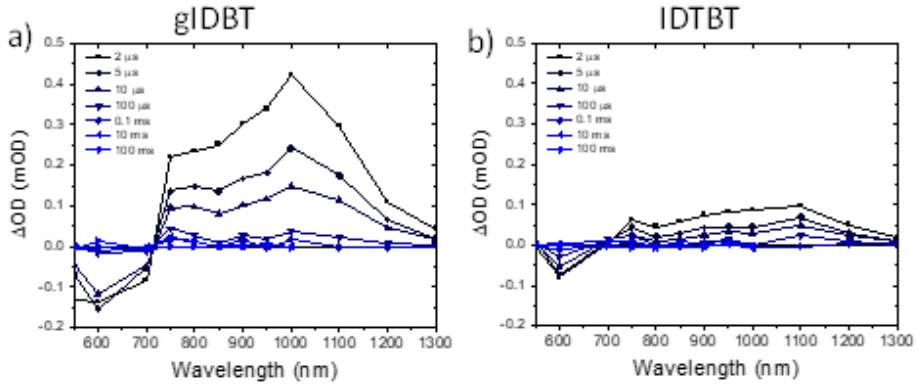

Figure S8. Transient absorption spectra of a) gIDTBT and b) IDTBT NPs at different delay times, excited at 650 nm (250 μJ cm^{-2}).

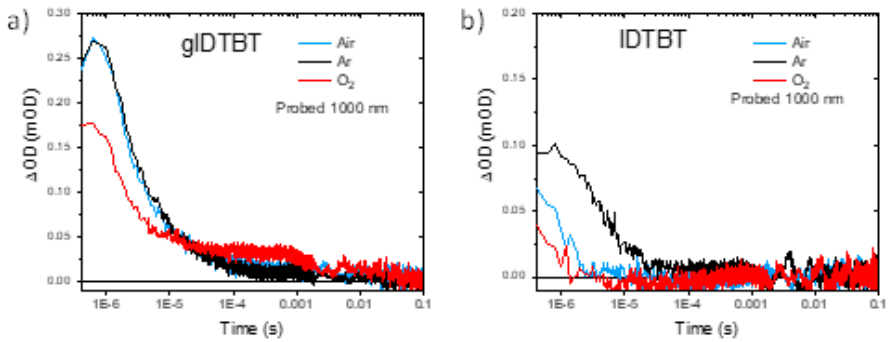

Figure S9. Transient absorption decay kinetics of a) gIDTBT and b) IDTBT NPs under Air, Argon, and Oxygen atmosphere, measured using excitation at 650 nm (50 μJ cm^{-2}) and a probe wavelength of 1000 nm. In presence of oxygen the transient absorption amplitude of gIDTBT decrease and exhibited a slow decay consistent with long-lived gIDTBT polaron due to superoxide formation.

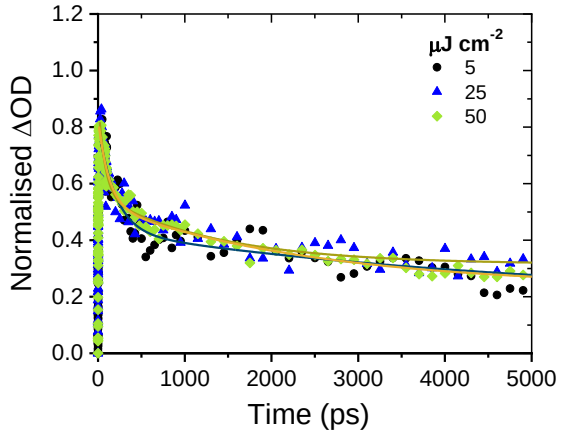

Figure S10. Deconvoluted transient absorption kinetics of gIDTBT polaron at different pump fluences from global analysis.

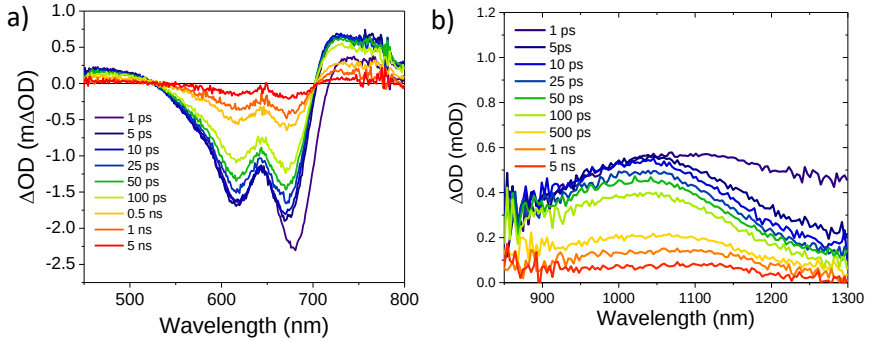

Figure S11. Ultrafast transient absorption spectra of IDTBT:OIDTBR NPs at different delay times, excited at 650 nm (5 μJ cm^{-2}) and probed in: a) the visible region and b) NIR region.

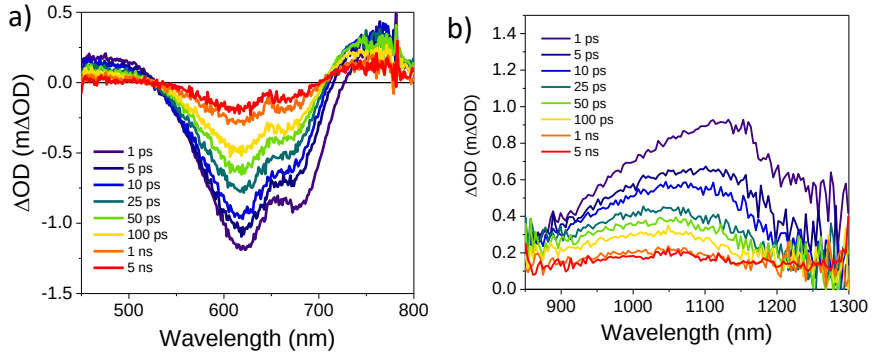

Figure S12. Ultrafast transient absorption spectra of gIDTBT:OIDTBR NPs at different delay times, excited at 650 nm (5 μJ cm^{-2}) and probed in: a) the visible region and b) NIR region.

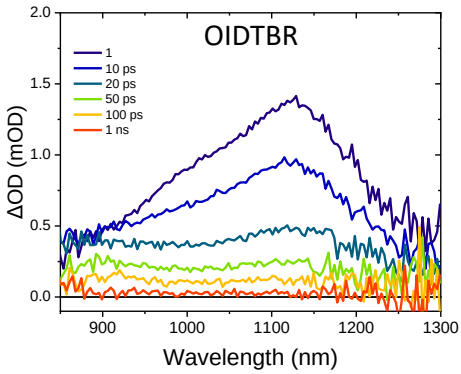

Figure S13. Ultrafast TAS spectra of neat OIDTBR NPs excited at 650 nm (5 μJ cm^{-2}) and probed in the NIR region.

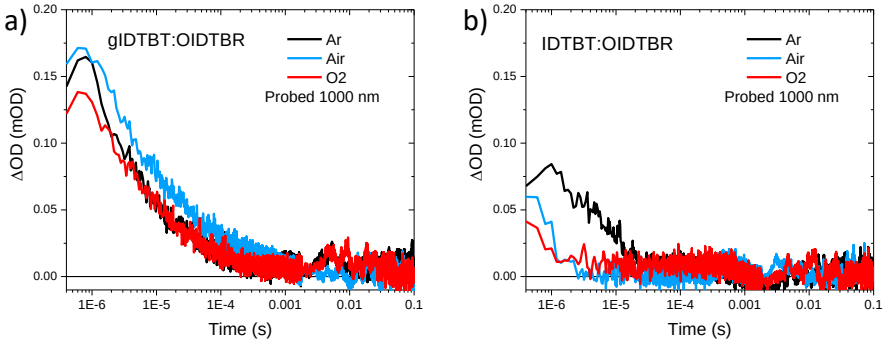

Figure S14. Transient absorption decay kinetics of a) gIDTBT:OIDTBR and b) IDTBT:OIDTBR NPs under Argon, Air and Oxygen atmosphere, measured using excitation at 650 nm (50 μJ cm-2) and a probe wavelength of 1000 nm.

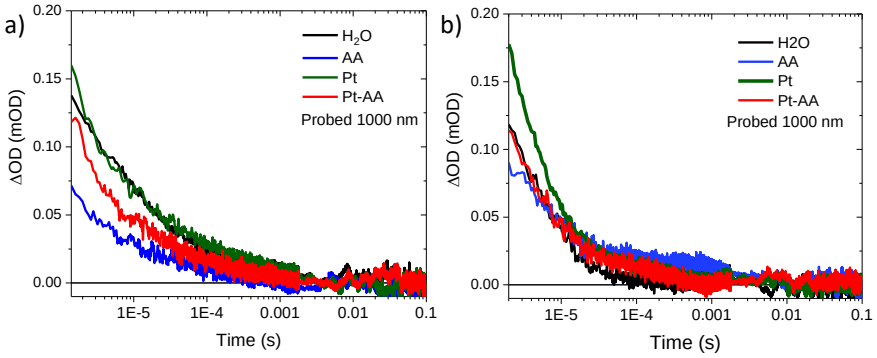

Figure S15. Transient absorption decay dynamics of a) gIDTBT:OIDTBR and b) IDTBT:OIDTBR probed at 1000 nm in absence of scavenger, with AA (0.2 M), Pt and in presence of both Pt and AA (0.2 M). Excitation at 650 nm (250 μJ cm^{-2}).

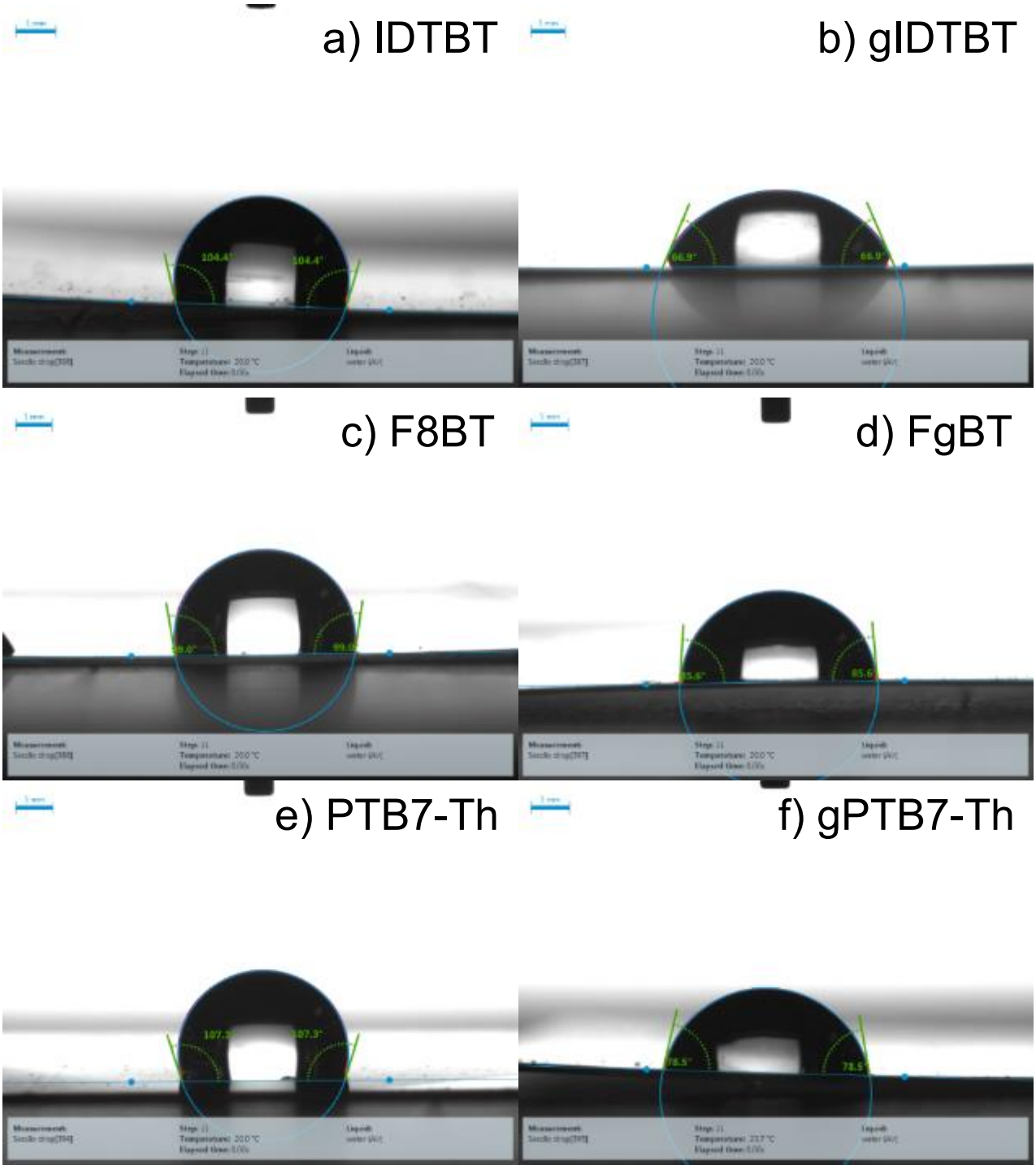

Figure S16: Water contact angle measurements performed on thin films of a) IDTBT, b) gIDTBT, c) F8BT, d) FgBT, e) PTB7-Th, f) gPTB7-Th.

Table S4: Contact angle measurements

Polymer	**Surface Free Energy (mN/m)**	**Disperse (mN/m)**	**Polar (mN/m)**	**Contact Angle (º)**	
				Water	**Ethylene Glycol**
F8BT	54.86 ±0.20	54.54 ±0.18	0.32 ±0.02	99.46 (±0.06)	61.26 (±0.02)
FgBT	48.10 ±0.42	47.16 ±0.37	0.94 ±0.06	85.91 (±0.14)	48.14 (±0.02)
IDTBT	24.36 ±0.21	23.98 ±0.19	0.38 ±0.02	104.51 (±0.02)	79.95 (±0.10)
gIDTBT	35.15 ±0.52	11.33 ±0.25	23.82 ±0.27	67.08 (±0.08)	47.96 (±0.23)
PTB7-Th	28.39 ±0.31	28.39 ±0.31	0.00 ±0.00	107.63 (±0.05)	80.71 (±0.14)
gPTB7-Th	29.52 ±0.59	18.83 ±0.38	10.70 ±0.20	78.56 (±0.07)	55.41 (±0.26)

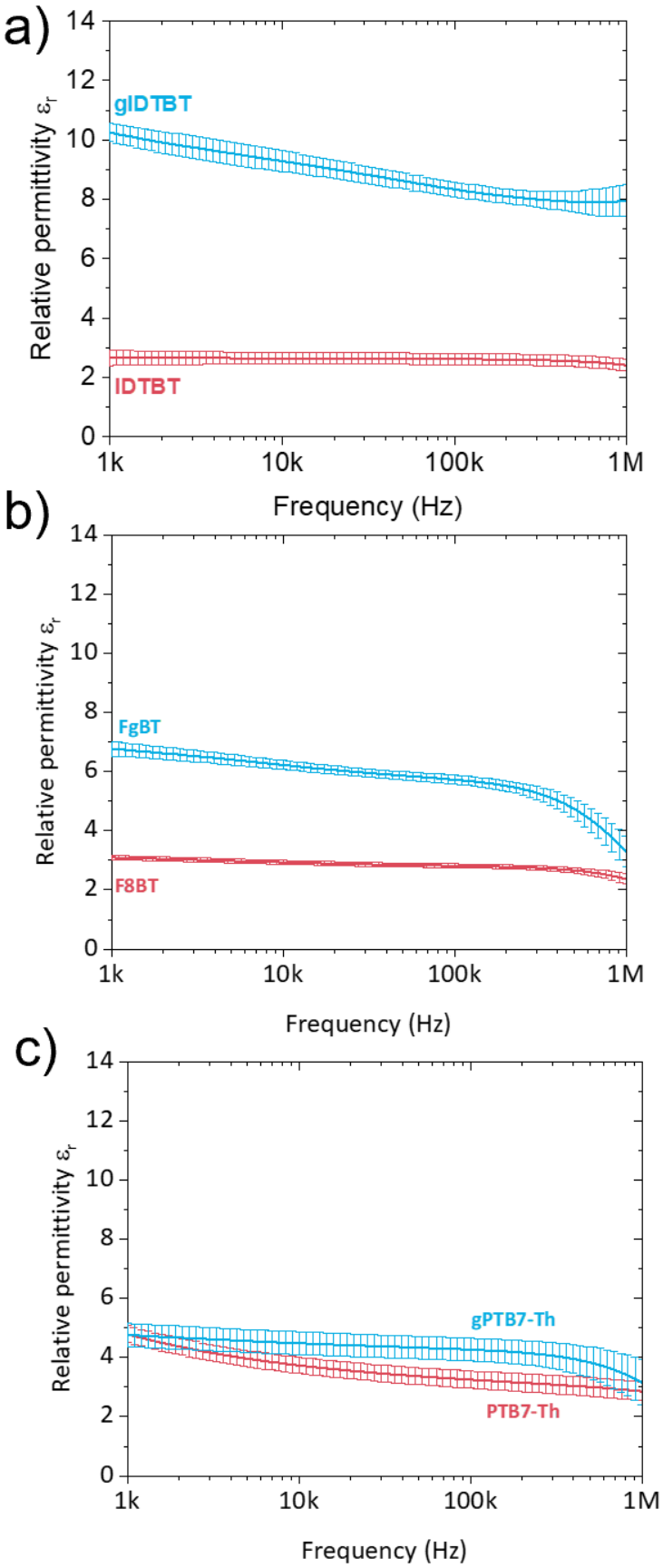

Figure S18: Frequency dependence of the relative permittivity between 1 kHz – 1MHz of a) IDTBT and gIDTBT, b) F8BT and FgBT, c) PTB7-Th and gPTB7-Th. The relative permittivities were measured for dry semiconductor films.

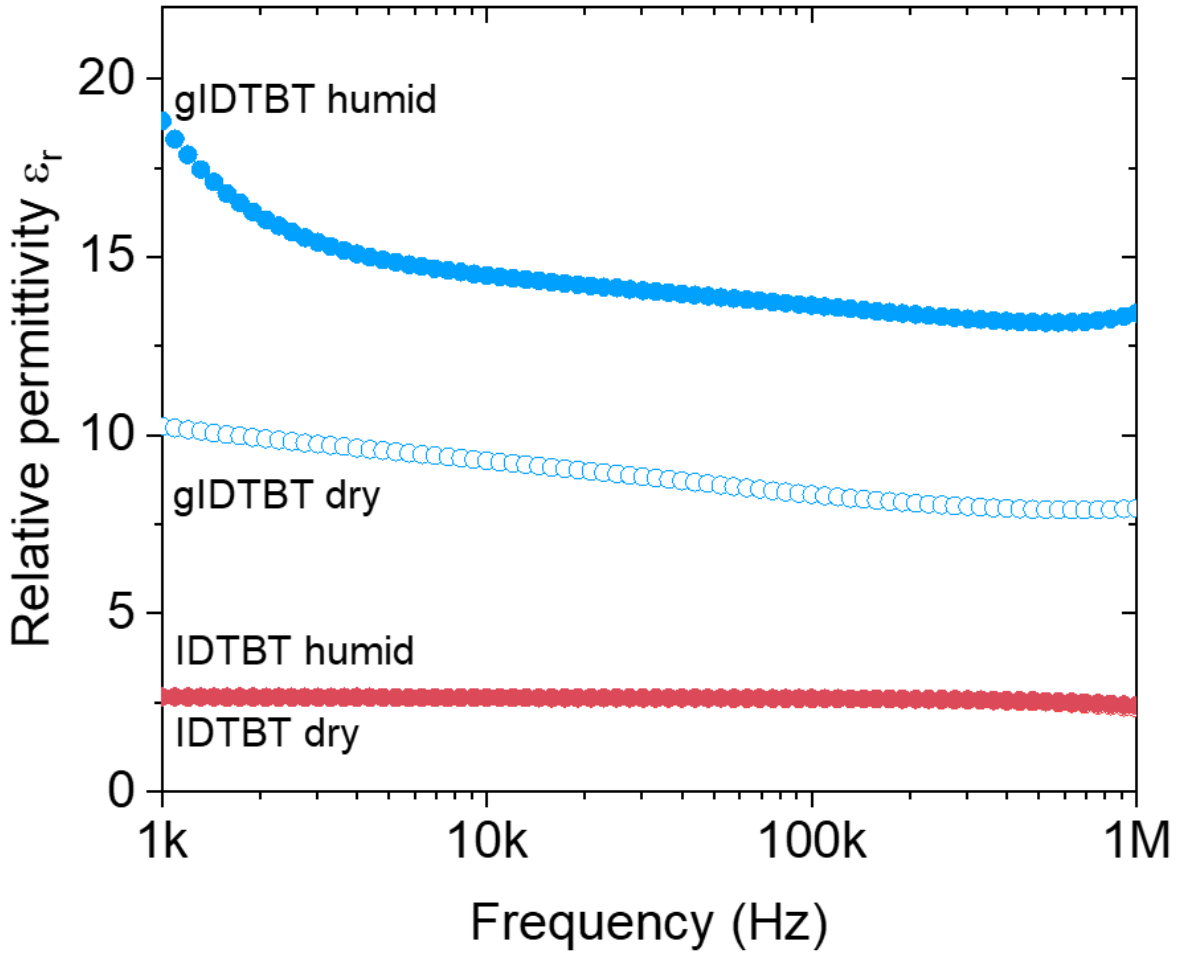

Figure S19: Frequency dependence of the relative permittivity of IDTBT and gIDTBT thin films exposed to dry (< 10% relative humidity) or humid (< 70% relative humidity) air.

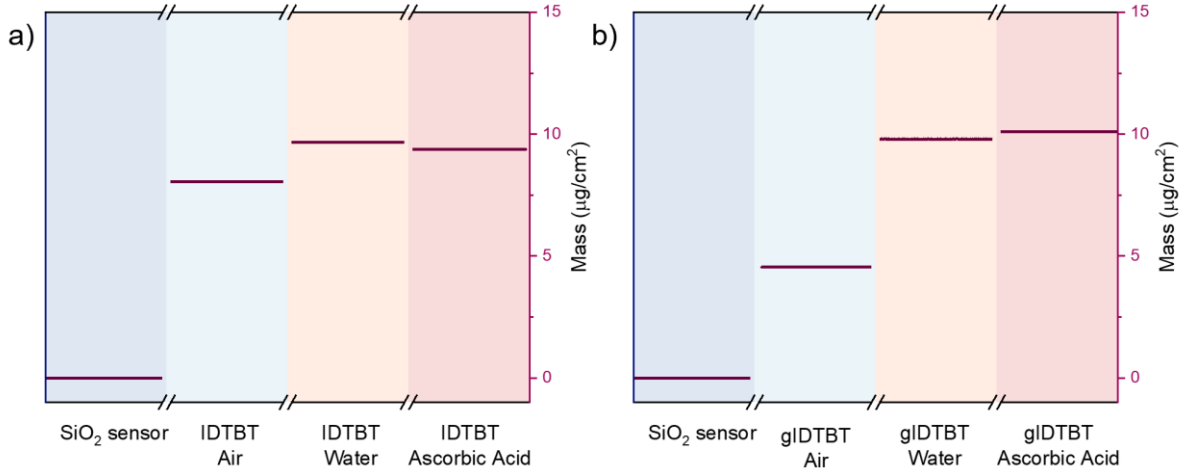

Figure S20: Quartz crystal microbalance measurements of the mass of thin films of a) IDTBT and b) gIDTBT suspended in air, water, or 0.2 M ascorbic acid.

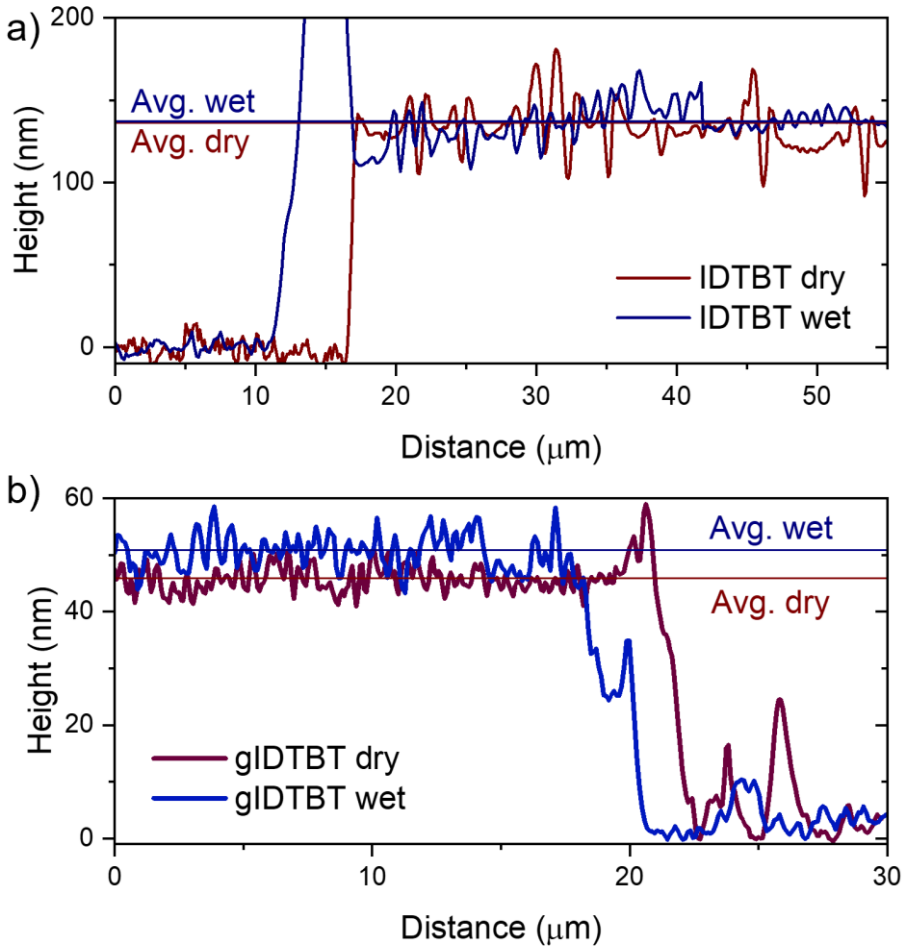

Figure S21: AFM height line cuts of films of a) IDTBT and b) gIDTBT before and after 24h water immersion. Water immersion had no effect on the thickness of the IDTBT film but caused the thickness of the gIDTBT film to increase by 11%. Note: The height averages are taken between 20-50 μm in panel a) and 0-15 μm in panel b).

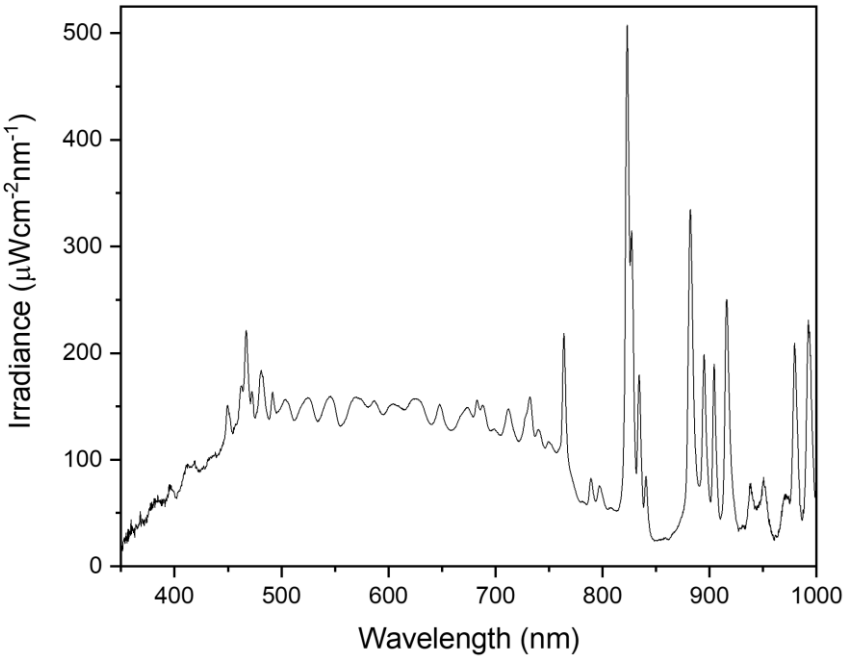

Figure S22: Irradiance spectrum of solar simulator used for H_2 evolution measurements.

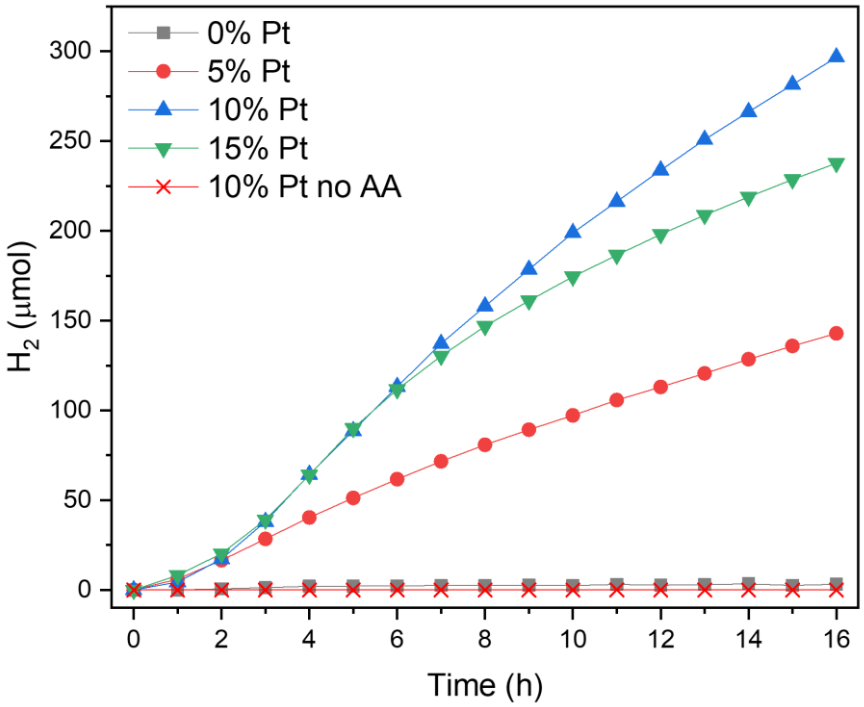

Figure S23: Optimisation of Pt loading. H_2 evolution vs. time of gIDTBT:oIDTBR NPs with different Pt loadings. H_2 evolution conditions: 1 mg nanoparticles, 0.2 mol l^{-1} ascorbic acid (12 ml), pH 2, AM1.5g solar simulator at 100 $mWcm^{-2}$ (1 sun), 4.41 cm^2 illumination area. Data presented are the average of 3 repeat runs.

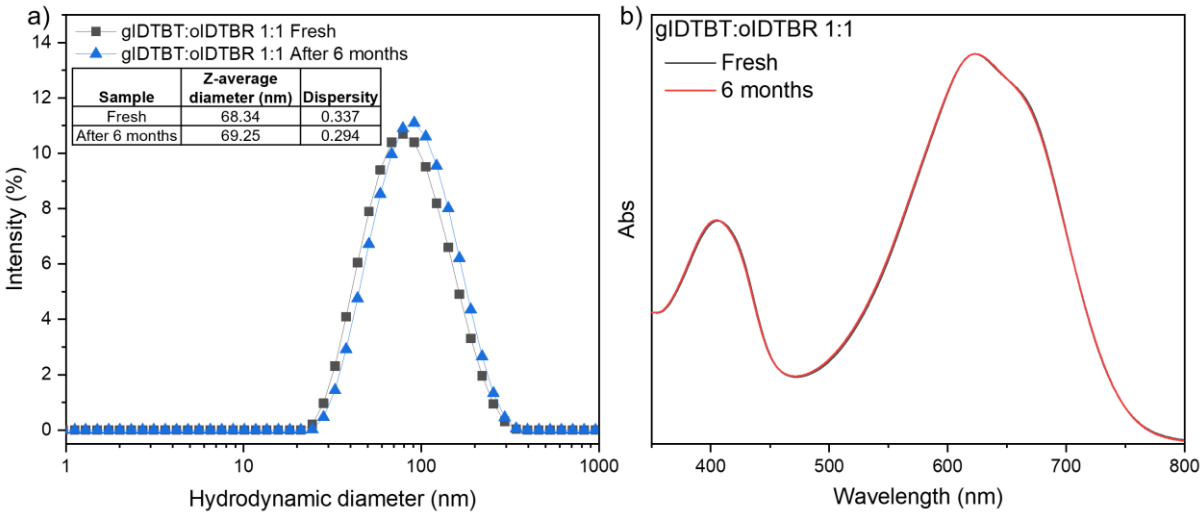

Figure S24: Stability of nanoparticle dispersions. **a)** Hydrodynamic size distributions, **b**) Normalized UV-Visible absorption spectra of gIDTBT:oIDTBR 1:1 NPs before and after 6 months of storage in the dark under ambient conditions. The UV-Vis spectrum and the size distribution of the NP sample remained unchanged.

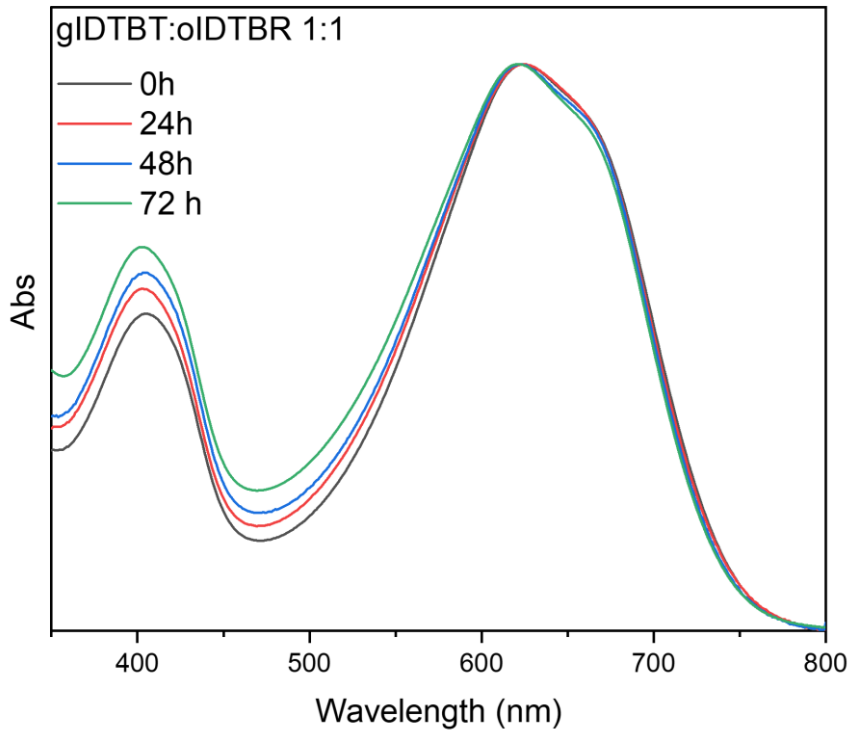

Figure S25: UV-Visible absorption spectrum of gIDTBT:oIDTBR 1:1 NPs as prepared and after various periods of H_2 evolution.

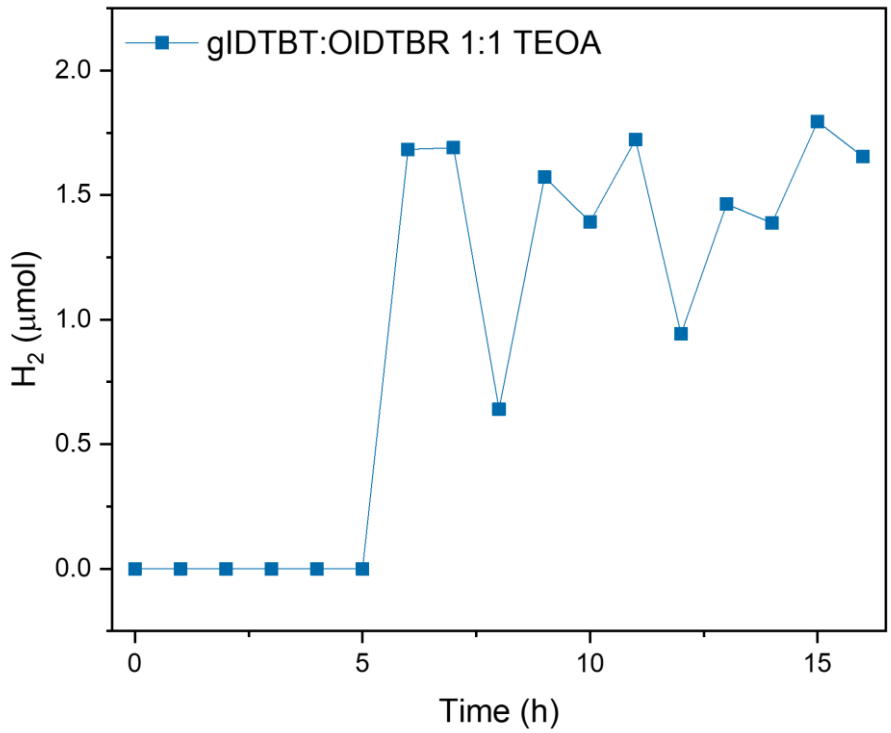

Figure S26: H_2 evolution vs. time of gIDTBT:oIDTBR 1:1 NPs in the presence of triethanolamine (TEOA) as the sacrificial hole scavenger. H_2 evolution conditions: 1 mg nanoparticles, 20 vol% TEOA in H_2O (12 ml), pH 10, AM1.5g solar simulator at 100 $mWcm^{-2}$ (1 sun), 4.41 cm^2 illumination area.

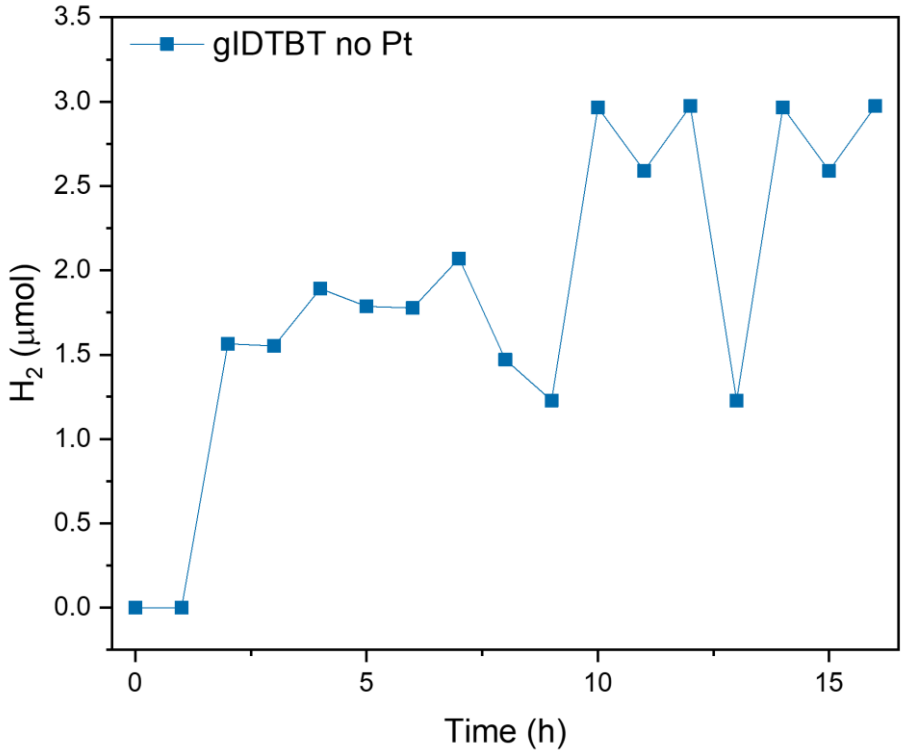

Figure S27: H_2 evolution vs. time of gIDTBT NPs in the absence of the Pt co-catalyst. H_2 evolution conditions: 1 mg nanoparticles, 0.2 mol l^{-1} ascorbic acid (12 ml), pH 2, AM1.5g solar simulator at 100 $mWcm^{-2}$ (1 sun), 4.41 cm^2 illumination area.

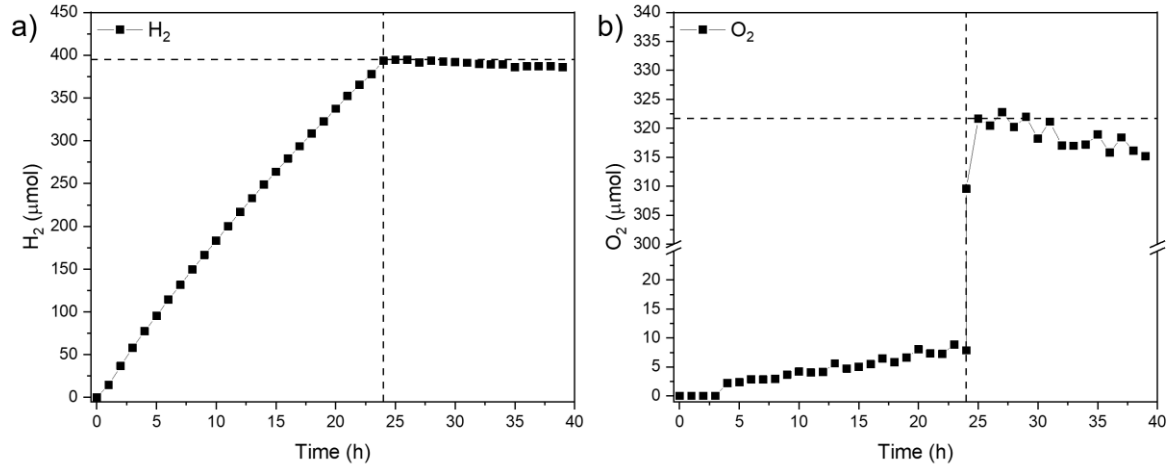

Figure S28: The effect of O_2 leakage on the H_2 evolution rate. The total amount of a) H_2 and b) O_2 present in the photocatalytic reactor during a run in which gIDTBT:oIDTBR 1:1 NPs were initially irradiated for 24 h (indicated by vertical dashed lines), after which time the light was switched off and the reactor was briefly opened to let in atmospheric O_2. The reactor was sealed and the sample was kept in the dark for a further 15 h. The horizontal dashed lines indicate the amounts of H_2 and O_2 preset in the reactor immediately after the reactor was opened. H_2 evolution conditions: 1 mg nanoparticles, 0.2 mol l^{-1} ascorbic acid (12 ml), pH 2, AM1.5g solar simulator at 100 $mWcm^{-2}$ (1 sun), 4.41 cm^2 illumination area.

The photocatalytic reactor is not perfectly airtight and during the H_2 evolution reaction a small amount of atmospheric O_2 gradually enters the reactor (Figure S28b). We hypothesized that the presence of O_2 in the reactor may lead to the oxygen reduction reaction (ORR) competing with the H_2 evolution reaction (HER) and the gradual increase in the O_2 concentration in the reactor would therefore lead to the gradual decrease in the HER rate observed throughout most runs. To test this hypothesis, we measured the amounts of O_2 and H_2 present in the reactor during a run in which gIDTBT:oIDTBR 1:1 NPs were initially irradiated for 24 h after which time the light was switched off and the reactor was briefly opened to let in atmospheric O_2. The amounts of O_2 and H_2 present in the reactor were then monitored for a further 15 h. After the light was switched off and extra O_2 was introduced into the reactor, the total amounts of O_2 and H_2 present in the reactor slowly decreased, as indicated by the dashed horizontal lines in figure S28. This suggests that the ORR may indeed be occurring. However, a much greater decrease in the H_2 concentration in the presence of O_2 would be expected if the ORR was the only mechanism responsible for the nonlinearity in the HER rates observed over 16 h. Figures S29-30 suggest that the depletion of AA and/or the accumulation of AA decomposition products contribute more strongly to the nonlinearity.

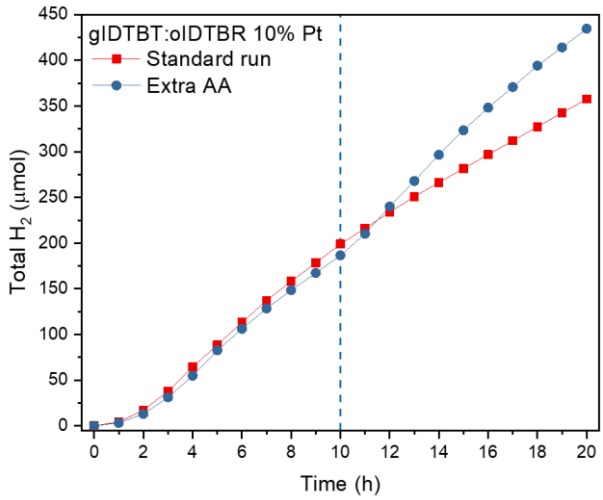

Figure S29: The total amount of H_2 evolved vs. time of gIDTBT:oIDTBR 1:1 NPs during a standard run in which the reactor remained sealed, and during a run in which the reactor was purged with Ar and extra AA (1.2 mmol) was added to the NP suspension after 10 h of H_2 evolution.

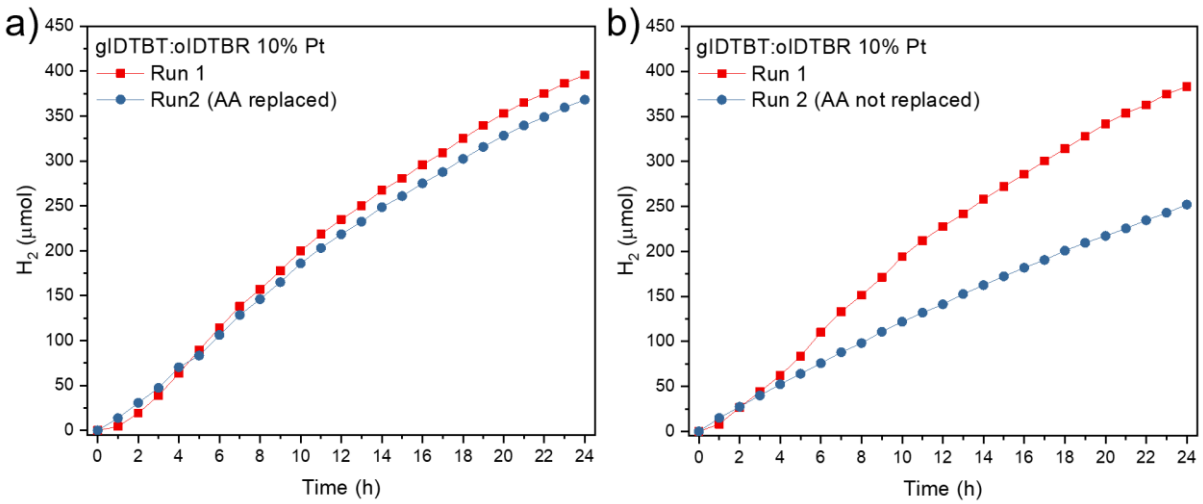

Figure S30: H_2 evolution vs. time of gIDTBT:oIDTBR 1:1 NPs during two consecutive 24 h runs. a) After the first run, the reactor was purged with Ar and the NPs were isolated using a centrifugal filter and added to a fresh solution of 0.2 M AA. b) After the first run, the reactor was purged with Ar and no further AA was added to the suspension. H_2 evolution conditions: 1 mg nanoparticles, 0.2 mol l^{-1} AA (12 ml), pH 2, AM1.5g solar simulator at 100 mWcm^{-2} (1 sun), 4.41 cm^2 illumination area.

The addition of extra AA into the reactor after 10 h of H_2 evolution resulted in an increased HER rate after 10 h compared to a standard run which displayed a gradual decrease in the HER rate over the 20 h reaction period (Figure S29). Furthermore, replacing the 0.2 M AA solution after 24 h of H_2 evolution resulted in an almost full recovery of the HER rate in the second 24 h run compared to the first 24 h run (Figure S30a) whereas the HER rate dropped substantially in the second run if the AA was not replaced. Together these data suggest that the dominant cause of the nonlinearity in the HER rates observable over 16-24 h is the gradual depletion of AA over the course of each run, which is consistent with previously reported data.[26] Nevertheless, the gIDTBT:oIDTBR 1:1 NPs display signs of degradation after 24 h of H_2 evolution (Figure S25) and further work is required to understand their degradation mechanisms and improve stability for practical applications.

References

[1] Q. Wang, K. Domen, *Chem. Rev.* **2020**, *120*, 919.

[2] J. Schneider, M. Matsuoka, M. Takeuchi, J. Zhang, Y. Horiuchi, M. Anpo, D. W. Bahnemann, *Chem. Rev.* **2014**, *114*, 9919.

[3] M. Ni, M. K. H. Leung, D. Y. C. Leung, K. Sumathy, *Renew. Sustain. Energy Rev.* **2007**, *11*, 401.

[4] P. Yohan, H. Takashi, D. Kazunari, in *Curr. Dev. Photocatal. Photocatalytic Mater.*, Elsevier, **2020**, pp. 141–157.

[5] T. Takata, J. Jiang, Y. Sakata, M. Nakabayashi, N. Shibata, V. Nandal, K. Seki, T. Hisatomi, K. Domen, *Nature* **2020**, *581*, 411.

[6] G. Zhang, L. Lin, G. Li, Y. Zhang, A. Savateev, S. Zafeiratos, X. Wang, M. Antonietti, *Angew. Chemie Int. Ed.* **2018**, *57*, 9372.

[7] S. Yang, Y. Gong, J. Zhang, L. Zhan, L. Ma, Z. Fang, R. Vajtai, X. Wang, P. M. Ajayan, *Adv. Mater.* **2013**, *25*, 2452.

[8] X. Wang, K. Maeda, A. Thomas, K. Takanabe, G. Xin, J. M. Carlsson, K. Domen, M. Antonietti, *Nat. Mater.* **2009**, *8*, 76.

[9] B. A. Pinaud, J. D. Benck, L. C. Seitz, A. J. Forman, Z. Chen, T. G. Deutsch, B. D. James, K. N. Baum, G. N. Baum, S. Ardo, H. Wang, E. Miller, T. F. Jaramillo, *Energy Environ. Sci.* **2013**, *6*, 1983.

[10] S. Yanagida, A. Kabumoto, K. Mizumoto, C. Pac, K. Yoshino, *J. Chem. Soc. Chem. Commun.* **1985**, *0*, 474.

[11] M. Sachs, R. S. Sprick, D. Pearce, S. A. J. Hillman, A. Monti, A. A. Y. Guilbert, N. J. Brownbill, S. Dimitrov, X. Shi, F. Blanc, M. A. Zwijnenburg, J. Nelson, J. R. Durrant, A. I. Cooper, *Nat. Commun.* **2018**, *9*, 4968.

[12] F. Vilela, K. Zhang, M. Antonietti, *Energy Environ. Sci.* **2012**, *5*, 7819.

[13] P. Guiglion, C. Butchosa, M. A. Zwijnenburg, *Macromol. Chem. Phys.* **2016**, *217*, 344.

[14] V. S. Vyas, V. W. Lau, B. V. Lotsch, *Chem. Mater.* **2016**, *28*, 5191.

[15] F. Beuerle, B. Gole, *Angew. Chemie - Int. Ed.* **2018**, *57*, 4850.

[16] T. Banerjee, K. Gottschling, G. Savasci, C. Ochsenfeld, B. V. Lotsch, *ACS Energy Lett.* **2018**, *3*, 400.

[17] X. Feng, X. Ding, D. Jiang, *Chem. Soc. Rev.* **2012**, *41*, 6010.

[18] J. Kosco, F. Moruzzi, B. Willner, I. McCulloch, *Adv. Energy Mater.* **2020**, *10*, 2001935.

[19] Y. Bai, L. Wilbraham, B. J. Slater, M. A. Zwijnenburg, R. S. Sprick, A. I. Cooper, *J. Am. Chem. Soc.* **2019**, *141*, 9063.

[20] D. J. Woods, S. A. J. Hillman, D. Pearce, L. Wilbraham, L. Q. Flagg, W. Duffy, I. McCulloch, J. R. Durrant, A. A. Y. Guilbert, M. A. Zwijnenburg, R. S. Sprick, J. Nelson, A. I. Cooper, *Energy Environ. Sci.* **2020**, *13*, 1843.

[21] J. Kosco, M. Bidwell, H. Cha, T. Martin, C. T. Howells, M. Sachs, D. H. Anjum, S. Gonzalez Lopez, L. Zou, A. Wadsworth, W. Zhang, L. Zhang, J. Tellam, R. Sougrat, F. Laquai, D. M. DeLongchamp, J. R. Durrant, I. McCulloch, *Nat. Mater.* **2020**, *19*, 559.

[22] M. Sachs, H. Cha, J. Kosco, C. M. Aitchison, L. Francàs, S. Corby, C. L. Chiang, A. A. Wilson, R. Godin, A. Fahey-Williams, A. I. Cooper, R. S. Sprick, I. McCulloch, J. R. Durrant, *J. Am. Chem. Soc.* **2020**, *142*, 14574.

[23] X. Wang, L. Chen, S. Y. Chong, M. A. Little, Y. Wu, W.-H. Zhu, R. Clowes, Y. Yan, M. A. Zwijnenburg, R. S. Sprick, A. I. Cooper, *Nat. Chem.* **2018**, *10*, 1180.

[24] Y. Wang, A. Vogel, M. Sachs, R. S. Sprick, L. Wilbraham, S. J. A. Moniz, R. Godin, M. A. Zwijnenburg, J. R. Durrant, A. I. Cooper, J. Tang, *Nat. Energy* **2019**, *4*, 746.

[25] A. Wadsworth, Z. Hamid, J. Kosco, N. Gasparini, I. McCulloch, *Adv. Mater.* **2020**, *32*, 2001763.

[26] A. Liu, L. Gedda, M. Axelsson, M. Pavliuk, K. Edwards, L. Hammarström, H. Tian, *J.*

Am. Chem. Soc. **2021**, jacs. 0c12654.
[27] S. Torabi, F. Jahani, I. Van Severen, C. Kanimozhi, S. Patil, R. W. A. Havenith, R. C. Chiechi, L. Lutsen, D. J. M. Vanderzande, T. J. Cleij, J. C. Hummelen, L. J. A. Koster, *Adv. Funct. Mater.* **2015**, *25*, 150.
[28] B. Meng, J. Liu, L. Wang, *Polym. Chem.* **2020**, *11*, 1261.
[29] Z. Hu, Z. Wang, X. Zhang, H. Tang, X. Liu, F. Huang, Y. Cao, *iScience* **2019**, *13*, 33.
[30] N. Cho, C. W. Schlenker, K. M. Knesting, P. Koelsch, H. L. Yip, D. S. Ginger, A. K. Y. Jen, *Adv. Energy Mater.* **2014**, *4*, 1301857.
[31] A. A. Mohapatra, Y. Dong, P. Boregowda, A. Mohanty, A. Sadhanala, X. Jiao, A. Narayan, C. R. McNeill, J. R. Durrant, S. Patil, *J. Phys. Chem. C* **2021**, *125*, 6896.
[32] S. Sami, R. Alessandri, R. Broer, R. W. A. Havenith, *ACS Appl. Mater. Interfaces* **2020**, *12*, 17783.
[33] N. Koizumi, T. Hanai, *J. Phys. Chem.* **1956**, *60*, 1496.
[34] S. Trasatti, *J. Electroanal. Chem. Interfacial Electrochem.* **1986**, *209*, 417.
[35] K. Landfester, *Adv. Mater.* **2001**, *13*, 765.
[36] S. Holliday, R. S. Ashraf, A. Wadsworth, D. Baran, S. A. Yousaf, C. B. Nielsen, C.-H. Tan, S. D. Dimitrov, Z. Shang, N. Gasparini, M. Alamoudi, F. Laquai, C. J. Brabec, A. Salleo, J. R. Durrant, I. McCulloch, *Nat. Commun.* **2016**, *7*, 11585.
[37] T. H. Thomas, D. J. Harkin, A. J. Gillett, V. Lemaur, M. Nikolka, A. Sadhanala, J. M. Richter, J. Armitage, H. Chen, I. McCulloch, S. M. Menke, Y. Olivier, D. Beljonne, H. Sirringhaus, *Nat. Commun.* **2019**, *10*, 2614.
[38] Y. W. Soon, S. Shoaee, R. S. Ashraf, H. Bronstein, B. C. Schroeder, W. Zhang, Z. Fei, M. Heeney, I. McCulloch, J. R. Durrant, *Adv. Funct. Mater.* **2014**, *24*, 1474.
[39] D. Baran, N. Gasparini, A. Wadsworth, C. H. Tan, N. Wehbe, X. Song, Z. Hamid, W. Zhang, M. Neophytou, T. Kirchartz, C. J. Brabec, J. R. Durrant, I. McCulloch, *Nat. Commun.* **2018**, *9*, 2059.
[40] C.-H. Tan, A. Wadsworth, N. Gasparini, S. Wheeler, S. Holliday, R. S. Ashraf, S. D. Dimitrov, D. Baran, I. McCulloch, J. R. Durrant, *J. Phys. Chem. C* **2019**, *123*, 5826.
[41] N. Cho, C. W. Schlenker, K. M. Knesting, P. Koelsch, H.-L. Yip, D. S. Ginger, A. K.-Y. Jen, *Adv. Energy Mater.* **2014**, *4*, 1301857.
[42] G. Zhang, T. M. Clarke, A. J. Mozer, *J. Phys. Chem. C* **2016**, *120*, 7033.
[43] M. Lenes, F. B. Kooistra, J. C. Hummelen, I. Van Severen, L. Lutsen, D. Vanderzande, T. J. Cleij, P. W. M. Blom, *J. Appl. Phys.* **2008**, *104*, 114517.
[44] X. Chen, Z. Zhang, Z. Ding, J. Liu, L. Wang, *Angew. Chemie Int. Ed.* **2016**, *55*, 10376.
[45] J. Brebels, J. V. Manca, L. Lutsen, D. Vanderzande, W. Maes, *J. Mater. Chem. A* **2017**, *5*, 24037.
[46] A. Nistor, G. Stiubianu, C. Racles, M. Cazacu, *Evaluation of the Water Sorption Capacity of Some Polymeric Materials by Dynamic Vapour Sorption*, **2011**.
[47] K. C. Ng, M. Burhan, M. W. Shahzad, A. Bin Ismail, *Sci. Rep.* **2017**, *7*, 1.
[48] M. Moser, T. C. Hidalgo, J. Surgailis, J. Gladisch, S. Ghosh, R. Sheelamanthula, Q. Thiburce, A. Giovannitti, A. Salleo, N. Gasparini, A. Wadsworth, I. Zozoulenko, M. Berggren, E. Stavrinidou, S. Inal, I. McCulloch, *Adv. Mater.* **2020**, *32*, 2002748.
[49] M. Nikolka, I. Nasrallah, B. Rose, M. K. Ravva, K. Broch, A. Sadhanala, D. Harkin, J. Charmet, M. Hurhangee, A. Brown, S. Illig, P. Too, J. Jongman, I. McCulloch, J. L. Bredas, H. Sirringhaus, *Nat. Mater.* **2017**, *16*, 356.
[50] A. Andryieuski, S. M. Kuznetsova, S. V. Zhukovsky, Y. S. Kivshar, A. V. Lavrinenko, *Sci. Rep.* **2015**, *5*, 1.
[51] N. Shinyashiki, S. Sudo, W. Abe, S. Yagihara, *J. Chem. Phys.* **1998**, *109*, 9843.
[52] W. Zhang, J. Smith, S. E. Watkins, R. Gysel, M. McGehee, A. Salleo, J. Kirkpatrick, S. Ashraf, T. Anthopoulos, M. Heeney, I. McCulloch, *J. Am. Chem. Soc.* **2010**, *132*, 11437.

[53] J. Kosco, I. McCulloch, *ACS Energy Lett.* **2018**, *3*, 2846.
[54] R. Hooper, L. J. Lyons, M. K. Mapes, D. Schumacher, D. A. Moline, R. West, *Macromolecules* **2001**, *34*, 931.
[55] L. Dong, S. Shen, H. Lu, S. Jin, J. Zhang, *ACS Sensors* **2019**, *4*, 1222.
[56] M. Qureshi, K. Takanabe, *Chem. Mater.* **2017**, *29*, 158.